Theory of pressure acoustics with viscous boundary layers and streaming in curved elastic cavities

Bach, Jacob Søberg; Bruus, Henrik

Published in:
Journal of the Acoustical Society of America

Link to article, DOI:
10.1121/1.5049579

Publication date:
2018

Document Version
Publisher's PDF, also known as Version of record

Theory of pressure acoustics with viscous boundary layers and streaming in curved elastic cavities

Jacob S. Bach, and Henrik Bruus

Citation: The Journal of the Acoustical Society of America **144**, 766 (2018); doi: 10.1121/1.5049579
View online: https://doi.org/10.1121/1.5049579
View Table of Contents: http://asa.scitation.org/toc/jas/144/2
Published by the Acoustical Society of America

Theory of pressure acoustics with viscous boundary layers and streaming in curved elastic cavities

Jacob S. Bach and Henrik Bruus[a)]
Department of Physics, Technical University of Denmark, DTU Physics Building 309, DK-2800 Kongens Lyngby, Denmark

(Received 22 April 2018; revised 6 July 2018; accepted 20 July 2018; published online 17 August 2018)

The acoustic fields and streaming in a confined fluid depend strongly on the viscous boundary layer forming near the wall. The width of this layer is typically much smaller than the bulk length scale set by the geometry or the acoustic wavelength, which makes direct numerical simulations challenging. Based on this separation in length scales, the classical theory of pressure acoustics is extended by deriving a boundary condition for the acoustic pressure that takes viscous boundary-layer effects fully into account. Using the same length-scale separation for the steady second-order streaming, and combining it with time-averaged short-range products of first-order fields, the usual limiting-velocity theory is replaced with an analytical slip-velocity condition on the long-range streaming field at the wall. The derived boundary conditions are valid for oscillating cavities of arbitrary shape and wall motion, as long as both the wall curvature and displacement amplitude are sufficiently small. Finally, the theory is validated by comparison with direct numerical simulation in two examples of two-dimensional water-filled cavities: The well-studied rectangular cavity with prescribed wall actuation, and a more generic elliptical cavity embedded in an externally actuated rectangular elastic glass block.
https://doi.org/10.1121/1.5049579

[PLM] Pages: 766–784

I. INTRODUCTION

The study of ultrasound effects in fluids in sub-millimeter cavities and channels has intensified the past decade, as microscale acoustofluidic devices are used increasingly in biology, environmental and forensic sciences, and clinical diagnostics.[1,2] Examples include cell synchronization,[3] enrichment of prostate cancer cells in blood,[4] size-independent sorting of cells,[5] manipulation of *C. elegans*,[6] and single-cell patterning.[7] Acoustics can also be used for non-contact microfluidic trapping and particle enrichment[8–10] as well as acoustic tweezing.[11–14]

The two fundamental physical phenomena that enable these microscale acoustofluidic applications are rooted in nonlinear acoustics. One fundamental phenomenon is the acoustic radiation force, which tends to focus suspended particles in the pressure nodes based on their acoustic contrast to the surrounding fluid.[15–21] The second fundamental phenomenon is the acoustic streaming appearing as steady flow rolls which tend to defocus suspended particles due to the Stokes drag.[22–27] Because the acoustic radiation force scales with the volume of the suspended particle, and the Stokes drag with its radius, the former dominates for large particles and the latter for small. For water at room temperature and 1 MHz ultrasound, the critical particle radius for the crossover between these two regimes has been determined to be around 2 μm.[28,29]

So far, the vast majority of successful microscale acoustofluidics applications has been for large (above 2 μm) particles, such as cells, whose dynamics is dominated by the well-characterized, robust acoustic radiation force, which depends on the bulk properties of the acoustic field and material parameters of the particles and the surrounding fluid. However, there is a strong motivation to handle also sub-micrometer particles such as bacteria, exosomes, and viruses, for use in contemporary lab-on-a-chip-based diagnostics and biomedical research.[9,30–32] In contrast to large particles, the dynamics of small (sub-micrometer) particles is dominated by the drag force from the ill-characterized acoustic streaming. To control the handling of such nanoparticle suspensions, a deeper understanding of the often complicated acoustic streaming is called for.

One important aspect of ultrasound acoustics is the large velocity gradients in the sub-micrometer-thin viscous boundary layer near rigid boundaries.[22] The shear stress and the Reynolds stress that build up in this region are responsible for the viscous damping of the acoustic fields and for the acoustic streaming, respectively. In water with kinematic viscosity $\nu_0 \approx 10^{-6}\,\mathrm{m}^2/\mathrm{s}$ at the frequency $f = (1/2\pi)\omega \approx 1$ MHz, the thickness $\delta = \sqrt{2\nu_0/\omega}$ of this boundary layer is on the order of 500 nm, while the acoustic wavelength is around 1.5 mm. This three-orders-of-magnitude separation of physically relevant length scales poses a severe challenge for numerical simulations. To circumvent the problem of resolving the thin boundary layer, we develop a theory were analytical solutions for the boundary layers are used to formulate boundary conditions for the pressure field and bulk streaming field, which both varies on the much longer length scale $d \gg \delta$.

First, we extend the classical pressure acoustics theory by formulating a boundary condition for the acoustic pressure that includes the presence of the boundary layer, which

a)Electronic mail: bruus@fysik.dtu.dk

is otherwise neglected. Thus, our extended boundary condition takes into account important effect of the boundary layer, such as increased viscous damping, shifts in resonance frequencies, and shear stresses on the surrounding walls.

Second, we formulate a generalized slip-velocity boundary condition for bulk acoustic streaming over curved oscillating surfaces. An important step in this direction was the development of the limiting-velocity theory by Nyborg in 1958 for perpendicularly oscillating curved walls.[33] Later modifications of this theory comprise modifications to the analysis in curvilinear coordinates by Lee and Wang in 1989,[34] and the treatment of oscillations in any direction for flat walls by Vanneste and Bühler in 2011.[35] Here, we extend these theories to harmonic oscillations in any direction of an arbitrarily shaped elastic wall, provided that both the radius of curvature and the acoustic wavelength are much larger than the boundary layer length-scale δ, and that also the amplitude of the perpendicular surface vibration is much smaller than δ.

Notably, the theoretical description developed here allows us to perform numerical simulations of the linear and nonlinear acoustics in arbitrarily shaped liquid-filled cavities embedded in oscillating elastic solids. Examples and validation of such simulations for two-dimensional (2D) systems are presented in the final sections of this paper, while a study of three-dimensional (3D) systems is work in progress to be presented later.

II. WALL MOTION AND PERTURBATION THEORY

We consider a fluid domain Ω bounded by an elastic, oscillating solid, see Fig. 1. All acoustic effects in the fluid are generated by the fluid-solid interface that oscillates harmonically around its equilibrium position, denoted $\boldsymbol{s}_0$ or $\partial\Omega$, with an angular frequency ω. The instantaneous position $\boldsymbol{s}(\boldsymbol{s}_0, t)$ at time t of this interface (the wall), is described by the small complex displacement $\boldsymbol{s}_1(\boldsymbol{s}_0)\mathrm{e}^{-\mathrm{i}\omega t}$,

$$\boldsymbol{s}(\boldsymbol{s}_0, t) = \boldsymbol{s}_0 + \boldsymbol{s}_1(\boldsymbol{s}_0)\,\mathrm{e}^{-\mathrm{i}\omega t}. \tag{1}$$

In contrast to Muller and Bruus,[36] we do not study the transient phase leading to this steady oscillatory motion.

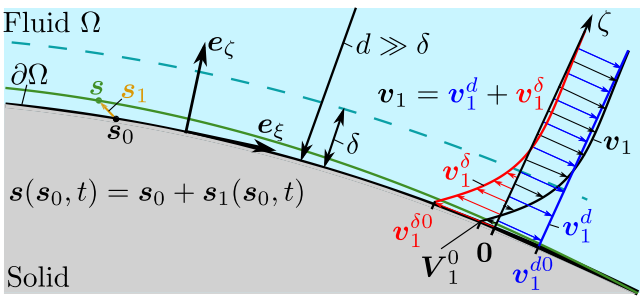

FIG. 1. (Color online) Sketch of the interface between a fluid (light blue, Ω) and a curved, oscillating solid (dark gray) with instantaneous position $\boldsymbol{s}$ (dark green line) and equilibrium position $\boldsymbol{s}_0$ (black line, $\partial\Omega$). The local curvilinear coordinate system on the interface is given by the tangent vectors $\boldsymbol{e}_\xi$ and $\boldsymbol{e}_\eta$ and the normal vector $\boldsymbol{e}_\zeta$. By a Helmholtz decomposition, the first-order acoustic fluid velocity $\boldsymbol{v}_1 = \boldsymbol{v}_1^d + \boldsymbol{v}_1^\delta$ is written as the sum of a long-range compressible part $\boldsymbol{v}_1^d$ (dark blue) extending into the bulk and a short-range incompressible part $\boldsymbol{v}_1^\delta$ (light red) with a decay length equal to the boundary-layer width δ. $\boldsymbol{V}_1^0 = \boldsymbol{v}_1^{d0} + \boldsymbol{v}_1^{\delta 0}$ is the Lagrangian velocity of the interface (the wall).

A. Fundamental conservation laws in acoustofluidics

The theory of acoustofluidics in Ω is derived from the conservation of the fluid mass and momentum density,

$$\partial_t \rho = -\boldsymbol{\nabla}\cdot(\rho\boldsymbol{v}), \tag{2a}$$

$$\partial_t(\rho\boldsymbol{v}) = -\boldsymbol{\nabla}\cdot[(\rho\boldsymbol{v})\boldsymbol{v}] + \boldsymbol{\nabla}\cdot\boldsymbol{\sigma}, \tag{2b}$$

where ρ is the mass density, $\boldsymbol{v}$ is the Eulerian fluid velocity, and $\boldsymbol{\sigma}$ is the viscous stress tensor, given by

$$\boldsymbol{\sigma} = -p\,\mathbf{I} + \boldsymbol{\tau}, \tag{2c}$$

$$\boldsymbol{\tau} = \eta_0^{\mathrm{b}}(\boldsymbol{\nabla}\cdot\boldsymbol{v})\mathbf{I} + \eta_0\left[\boldsymbol{\nabla}\boldsymbol{v} + (\boldsymbol{\nabla}\boldsymbol{v})^{\mathrm{T}} - \frac{2}{3}(\boldsymbol{\nabla}\cdot\boldsymbol{v})\mathbf{I}\right]. \tag{2d}$$

Here, p is the pressure and $\boldsymbol{\tau}$ is the viscous part of the stress tensor given in terms of the bulk viscosity η_0^{b}, the dynamic viscosity η_0, the identity matrix $\mathbf{I}$, and the superscript "T" denoting matrix transpose. Thermal dissipation is neglected throughout this work. We introduce the isentropic compressibility κ_0 and speed of sound c_0,

$$\kappa_0 = \frac{1}{\rho_0}\left(\frac{\partial\rho}{\partial p}\right)_S = \frac{1}{\rho_0 c_0^2}, \tag{3}$$

as well as the small dimensionless damping coefficient Γ in terms of the viscosity ratio β,

$$\Gamma = (\beta+1)\eta_0\omega\kappa_0, \quad \beta = \frac{\eta_0^{\mathrm{b}}}{\eta_0} + \frac{1}{3}. \tag{4}$$

B. Perturbation expansion

The linear acoustic response of the system is proportional to the displacement stimulus $\boldsymbol{s}_1(\boldsymbol{s}_0)\mathrm{e}^{-\mathrm{i}\omega t}$, and the resulting complex-valued quantities $Q_1(\boldsymbol{r})\,\mathrm{e}^{-\mathrm{i}\omega t}$ are called first-order fields with subscript "1". The physical time-dependent quantity $Q_1^{\mathrm{phys}}(\boldsymbol{r}, t)$ corresponding to Q_1 is given by the real part $Q_1^{\mathrm{phys}}(\boldsymbol{r}, t) = \mathrm{Re}[Q_1(\boldsymbol{r})\,\mathrm{e}^{-\mathrm{i}\omega t}]$.

As the governing equations are nonlinear, we also encounter higher-order terms, and in the present work, we include terms to second order in the stimulus. Moreover, since we are only interested in the steady part of these second-order fields, we let in the following the subscript "2" denote a time-averaged quantity, written as $Q_2(\boldsymbol{r}) = \langle Q_2(\boldsymbol{r}, t)\rangle = (\omega/2\pi)\int_0^{2\pi/\omega} Q_2(\boldsymbol{r}, t)\,\mathrm{d}t$. Time-averages of products of time-harmonic complex-valued first-order fields A_1 and B_1 are also of second order, and for those we have $\langle A_1 B_1\rangle = \frac{1}{2}\mathrm{Re}[A_1(\boldsymbol{r})B_1^*(\boldsymbol{r})]$, where the asterisk denote complex conjugation.

Using this notation for the fluid, we expand the mass density ρ, the pressure p, and the velocity $\boldsymbol{v}$ in perturbation series of the form

$$\rho = \rho_0 + \rho_1(\boldsymbol{r})\mathrm{e}^{-\mathrm{i}\omega t} + \rho_2(\boldsymbol{r}), \tag{5a}$$

$$p = p_0 + p_1(\boldsymbol{r})\mathrm{e}^{-\mathrm{i}\omega t} + p_2(\boldsymbol{r}), \tag{5b}$$

$$\boldsymbol{v} = \boldsymbol{0} + \boldsymbol{v}_1(\boldsymbol{r})\mathrm{e}^{-\mathrm{i}\omega t} + \boldsymbol{v}_2(\boldsymbol{r}), \tag{5c}$$

where $\rho_1 \ll \rho_0$, $p_1 = c_0^2\rho_1 \ll c_0^2\rho_0$, and $|\boldsymbol{v}_1| \ll c_0$. The subscripts 1 and 2 denote the order in the small acoustic Mach number $\mathrm{Ma} = (1/c_0)|\boldsymbol{v}_1|$, which itself is proportional to $\boldsymbol{s}_1$.

C. No-slip boundary condition at the wall

To characterize the wall motion, we compute the time derivative of $\boldsymbol{s}(\boldsymbol{s}_0, t)$ in Eq. (1),

$$\partial_t \boldsymbol{s}(\boldsymbol{s}_0, t) = -\mathrm{i}\omega \boldsymbol{s}_1(\boldsymbol{s}_0)\,\mathrm{e}^{-\mathrm{i}\omega t} = \boldsymbol{V}_1^0(\boldsymbol{s}_0)\,\mathrm{e}^{-\mathrm{i}\omega t}, \tag{6}$$

where $\boldsymbol{V}_1^0(\boldsymbol{s}_0) = -\mathrm{i}\omega \boldsymbol{s}_1(\boldsymbol{s}_0)$ is the Lagrangian velocity of the wall surface element with equilibrium position $\boldsymbol{s}_0$ and instantaneous position $\boldsymbol{s}$. The no-slip boundary condition on the Eulerian fluid velocity $\boldsymbol{v}(\boldsymbol{r}, t)$ is imposed at the instantaneous surface position $\boldsymbol{s}(t)$,[35,37]

$$\boldsymbol{v}(\boldsymbol{s}_0 + \boldsymbol{s}_1\mathrm{e}^{-\mathrm{i}\omega t}, t) = \boldsymbol{V}_1^0(\boldsymbol{s}_0)\,\mathrm{e}^{-\mathrm{i}\omega t}, \quad \text{no–slip condition.} \tag{7}$$

Combining Eqs. (5c) and (7) with the Taylor expansion $\boldsymbol{v}_1(\boldsymbol{s}_0 + \boldsymbol{s}_1, t) \approx \boldsymbol{v}_1(\boldsymbol{s}_0)\mathrm{e}^{-\mathrm{i}\omega t} + \langle(\boldsymbol{s}_1 \cdot \boldsymbol{\nabla})\boldsymbol{v}_1\rangle|_{\boldsymbol{s}_0}$, and collecting the terms order by order, gives

$$\boldsymbol{v}_1(\boldsymbol{s}_0) = \boldsymbol{V}_1^0(\boldsymbol{s}_0), \quad \text{1st–order condition,} \tag{8a}$$

$$\boldsymbol{v}_2(\boldsymbol{s}_0) = -\langle(\boldsymbol{s}_1 \cdot \boldsymbol{\nabla})\boldsymbol{v}_1\rangle|_{\boldsymbol{s}_0}, \quad \text{2nd–order condition.} \tag{8b}$$

Note that the expansion, or Stokes drift, in Eq. (8b) is valid, if the length scale over which $\boldsymbol{v}_1$ varies is much larger than $|\boldsymbol{s}_1|$. So we require $|\boldsymbol{s}_{1\parallel}| \ll d$ and $|\boldsymbol{s}_{1\zeta}| \ll \delta$.

D. The limit of weakly curved, thin boundary layers

The crux of our work is the analytical treatment of weakly curved, thin viscous boundary layers. This notion is quantified using the boundary-layer length scale δ and the compressional length scale d,

$$\delta = \sqrt{\frac{2\nu_0}{\omega}}, \quad d = \min\{k_0^{-1}, R\}, \tag{9}$$

where d is the minimum of the wavelength scale $k_0^{-1} = c_0/\omega$ and the length scale R over which the surface curves. We express our subsequent analysis to lowest order in ϵ, defined as the ratio of these length scales,

$$\epsilon = \frac{\delta}{d} \ll 1, \tag{10}$$

where the inequality holds in the limit of weakly curved ($\delta/R \ll 1$), thin boundary layers ($k_0\delta \ll 1$), a condition usually satisfied in microfluidic devices.

E. Local boundary-layer coordinates

The limit $\epsilon \ll 1$ allows for drastic simplifications of the otherwise complex analytical expressions for curvilinear derivatives of fields inside the boundary layers at distances of order δ or smaller from the wall. To see this, we introduce the local, right-handed, orthogonal, curvilinear coordinate system with coordinates ξ, η, and ζ. The latter measures distance away from the surface equilibrium position along the surface unit normal vector $\boldsymbol{e}_\zeta$, while the tangential coordinates ξ and η increase in the respective directions of the unit tangent vectors $\boldsymbol{e}_\xi$ and $\boldsymbol{e}_\eta$, but not necessarily measuring arc length, see Fig. 1. To make the scale R of the curved surface explicit, we use the vectorial notation for curvilinear derivatives and introduce the differential-geometric symbols employed in previous boundary-layer analyses in the literature,[33,34]

$$\begin{aligned} &h_i = |\partial_i \boldsymbol{r}|, \quad T_{kji} = \left(\tilde{\partial}_k \boldsymbol{e}_j\right) \cdot \boldsymbol{e}_i, \quad \text{for } i,j,k = \xi,\eta,\zeta, \\ &\tilde{\partial}_i = \frac{1}{h_i}\partial_i, \quad \mathcal{H}_k = T_{iki} = \tilde{\partial}_k\left[\sum_{i\neq k} \log h_i\right]. \end{aligned} \tag{11}$$

Note that this is not covariant formulation, see Appendix A for details on the differential geometry. Because ζ measures arc length, we have $h_\zeta = 1$ and consequently $\tilde{\partial}_\zeta = \partial_\zeta$. The surface length scale can now be defined as $R \sim \min\{T_{kji}^{-1}, \mathcal{H}_k^{-1}\}$, which in many situations is comparable with the surface curvature radius.

F. Surface fields, boundary-layer fields, and bulk fields

For $\epsilon \ll 1$, we may separate any field $\boldsymbol{A}$ inside the boundary layer in the perpendicular coordinate ζ,

$$\boldsymbol{A}(\xi,\eta,\zeta) = \boldsymbol{A}^0(\xi,\eta)\,a(\zeta), \quad \zeta \lesssim \delta \ll d. \tag{12}$$

Here, superscript "0" defines a surface field $\boldsymbol{A}^0(\xi,\eta) = \boldsymbol{A}(\xi,\eta,0)$, such as the wall velocity $\boldsymbol{V}_1^0$ and the fluid velocity $\boldsymbol{v}^0$ at the equilibrium position $\boldsymbol{s}_0$ of the wall. Note that a surface field does not have a perpendicular derivative, although it does have a perpendicular component. This coordinate separation results in the following expressions in vectorial notation for the divergence (A6) and advective derivative (A8) involving surface fields:

$$\boldsymbol{\nabla} \cdot \boldsymbol{A}^0 = \boldsymbol{\nabla}_\parallel \cdot \boldsymbol{A}_\parallel^0 + \mathcal{H}_\zeta A_\zeta^0, \tag{13a}$$

$$(\boldsymbol{A}^0 \cdot \boldsymbol{\nabla})\boldsymbol{B}^0 = \boldsymbol{A}_\parallel^0 \cdot (\boldsymbol{\nabla}_\parallel B_i^0)\,\boldsymbol{e}_i + A_k^0 B_j^0 T_{kji}\boldsymbol{e}_i, \tag{13b}$$

$$\boldsymbol{A}_\parallel = A_\xi\,\boldsymbol{e}_\xi + A_\eta\,\boldsymbol{e}_\eta, \tag{13c}$$

$$\boldsymbol{\nabla}_\parallel = \boldsymbol{e}_\xi\tilde{\partial}_\xi + \boldsymbol{e}_\eta\tilde{\partial}_\eta, \tag{13d}$$

where subscript "$\parallel$" denotes tangential components. See Appendix A for supplemental details.

Importantly, for fluid fields, we distinguish between bulk fields $\boldsymbol{A}^d$ that extend into the bulk with spatial variation on the compressional length scale d and that are typically found by numerical simulation, and boundary-layer fields $\boldsymbol{A}^\delta$ that decays to zero away from the wall at the boundary-layer length scale δ, as sketched in Fig. 1,

$$\boldsymbol{A}^\delta = \boldsymbol{A}^{\delta 0}(\xi,\eta)\,a^\delta(\zeta), \text{ with } a^\delta(\zeta) \to 0 \text{ for } \frac{\zeta}{\delta} \to \infty. \tag{14}$$

This specific property makes it possible to obtain analytical solutions for the boundary-layer fields $\boldsymbol{A}^\delta$, because the

surface-derivative quantities $\nabla_\parallel$, T_{kji}, and $\mathcal{H}_k$, all of size d^{-1}, are a factor of ϵ smaller than the perpendicular derivative ∂_ζ of size δ^{-1}, so they can be neglected. To lowest order in ϵ, as detailed further at the end of Appendix A, the curvilinear derivatives of scalar and vector boundary-layer fields thus simplify to

$$\nabla^2 g^\delta \approx \partial_\zeta^2 g^\delta, \tag{15a}$$

$$\nabla^2 \boldsymbol{A}^\delta \approx \boldsymbol{A}^{\delta 0}\partial_\zeta^2 a(\zeta) = \partial_\zeta^2 \boldsymbol{A}^\delta, \tag{15b}$$

$$\boldsymbol{\nabla}\cdot\boldsymbol{A}^\delta \approx \boldsymbol{\nabla}_\parallel\cdot\boldsymbol{A}_\parallel^\delta + \partial_\zeta A_\zeta^\delta. \tag{15c}$$

With Eqs. (13) and (15), we have established to leading order in ϵ the expressions in vectorial form for the curvilinear derivatives in the boundary layer necessary for the subsequent analytical treatment of the boundary layer. In summary, the length-scale conditions for our theory to be valid, in particular Eqs. (8) and (15), are

$$\delta \ll d, \quad |\boldsymbol{s}_{1\parallel}| \ll d, \quad |s_{1\zeta}| \ll \delta. \tag{16}$$

III. FIRST-ORDER TIME-HARMONIC FIELDS

Returning to the perturbation expansion (5), we write the first-order part of the governing equations (2),

$$p_1 = c_0^2\rho_1, \tag{17a}$$

$$-\mathrm{i}\omega\kappa_0 p_1 = -\boldsymbol{\nabla}\cdot\boldsymbol{v}_1, \tag{17b}$$

$$-\mathrm{i}\omega\rho_0\boldsymbol{v}_1 = -\boldsymbol{\nabla}[p_1 - \beta\eta_0\boldsymbol{\nabla}\cdot\boldsymbol{v}_1] + \eta_0\nabla^2\boldsymbol{v}_1, \tag{17c}$$

we make a standard Helmholtz decomposition of the velocity field $\boldsymbol{v}_1$,[21,33,34,37]

$$\boldsymbol{v}_1 = \boldsymbol{v}_1^d + \boldsymbol{v}_1^\delta, \quad \text{where } \boldsymbol{\nabla}\times\boldsymbol{v}_1^d = \boldsymbol{0} \text{ and } \boldsymbol{\nabla}\cdot\boldsymbol{v}_1^\delta = 0, \tag{18}$$

and insert it into Eq. (17). We separate the equations in solenoidal and irrotational parts and find

$$\mathrm{i}\omega\kappa_0 p_1 = \boldsymbol{\nabla}\cdot\boldsymbol{v}_1^d, \tag{19a}$$

$$-\mathrm{i}\omega\rho_0\boldsymbol{v}_1^d = \boldsymbol{\nabla}\cdot\boldsymbol{\sigma}_1^d = -(1-\mathrm{i}\Gamma)\boldsymbol{\nabla}p_1, \tag{19b}$$

$$-\mathrm{i}\omega\rho_0\boldsymbol{v}_1^\delta = \boldsymbol{\nabla}\cdot\boldsymbol{\sigma}_1^\delta = \eta_0\nabla^2\boldsymbol{v}_1^\delta. \tag{19c}$$

From this, we derive Helmholtz equations for the bulk fields p_1 and $\boldsymbol{v}_1^d$ as well as for the boundary-layer field $\boldsymbol{v}_1^\delta$,

$$\nabla^2 p_1 + k_\mathrm{c}^2 p_1 = 0, \quad \text{where } k_\mathrm{c} = \left(1+\mathrm{i}\frac{\Gamma}{2}\right)k_0, \tag{20a}$$

$$\nabla^2\boldsymbol{v}_1^d + k_\mathrm{c}^2\boldsymbol{v}_1^d = \boldsymbol{0}, \tag{20b}$$

$$\nabla^2\boldsymbol{v}_1^\delta + k_\mathrm{s}^2\boldsymbol{v}_1^\delta = \boldsymbol{0}, \quad \text{where } k_\mathrm{s} = \frac{1+\mathrm{i}}{\delta}. \tag{20c}$$

Here, we have introduced the compressional wavenumber k_c in terms of Γ defined in Eq. (4) and $k_0 = \omega/c_0$, and the shear wave number k_s in terms of δ. Note that Γ is of second order in ϵ,

$$\Gamma = \frac{1+\beta}{2}(k_0\delta)^2 \sim \epsilon^2 \ll 1. \tag{21}$$

From Eq. (19b) follows that the long-range velocity $\boldsymbol{v}_1^d$ is a potential flow proportional to $\boldsymbol{\nabla}p_1$, and as such it is the acoustic velocity of pressure acoustics. The short-range velocity $\boldsymbol{v}_1^\delta$ is confined to the thin boundary layer of width δ close to the surface, and therefore it is typically not observed in experiments and is ignored in classical pressure acoustics. In the following we derive an analytic solution for the boundary-layer field $\boldsymbol{v}_1^\delta$, which is used to determine a boundary condition for p_1. In this way, the viscous effects from the boundary layer are taken into account in computations of the long-range pressure-acoustic fields p_1 and $\boldsymbol{v}_1^d$.

A. Analytical form of the first-order boundary-layer field

By using Eq. (15b), the analytical solution $\boldsymbol{v}_1^\delta$ to Eq. (20c) is found to be

$$\boldsymbol{v}_1^\delta = \boldsymbol{v}_1^{\delta 0}(\xi,\eta)\,\mathrm{e}^{\mathrm{i}k_\mathrm{s}\zeta} + \mathcal{O}(\epsilon), \tag{22a}$$

which describes a shear wave heavily damped over a single wave length, as it travels away from the surface with speed $c_\mathrm{sw} = \omega\delta \ll c_0$. To satisfy the boundary condition (8a), we impose the following condition for $\boldsymbol{v}_1^{\delta 0}$ at the equilibrium position $\boldsymbol{s}_0$ of the wall,

$$\boldsymbol{v}_1^{\delta 0} = \boldsymbol{V}_1^0 - \boldsymbol{v}_1^{d0}, \quad \text{first–order no–slip condition.} \tag{22b}$$

B. Boundary condition for the first-order pressure field

We now derive a boundary condition for the first-order pressure field p_1, which takes the viscous boundary layer effects into account without explicit reference to $\boldsymbol{v}_1$. First, it is important to note that the incompressibility condition $\boldsymbol{\nabla}\cdot\boldsymbol{v}_1^\delta = 0$ used on Eq. (22a) leads to a small perpendicular short-range velocity at $\boldsymbol{s}_0$,

$$v_{1\zeta}^{\delta 0} = \frac{\mathrm{i}}{k_\mathrm{s}}\boldsymbol{\nabla}\cdot\boldsymbol{v}_1^{\delta 0} = \frac{\mathrm{i}}{k_\mathrm{s}}\boldsymbol{\nabla}\cdot\boldsymbol{V}_1^0 - \frac{\mathrm{i}}{k_\mathrm{s}}\boldsymbol{\nabla}\cdot\boldsymbol{v}_1^{d0}. \tag{23}$$

Because $k_\mathrm{s}^{-1} \simeq \delta$ and $\boldsymbol{\nabla}\cdot\boldsymbol{v}_1^{\delta 0} \simeq d^{-1}$, we find that $|v_{1\zeta}^{\delta 0}| \sim \epsilon|v_1| \ll |v_1|$. We repeatedly exploit this relation to neglect terms with $v_{1\zeta}^{\delta 0}$ in the following analyses to lowest order in ϵ. Using the no-slip condition (22b), the boundary condition on the long-range velocity becomes

$$v_{1\zeta}^{d0} = V_{1\zeta}^0 - v_{1\zeta}^{\delta 0} \tag{24a}$$

$$= \left(V_{1\zeta}^0 - \frac{\mathrm{i}}{k_\mathrm{s}}\boldsymbol{\nabla}\cdot\boldsymbol{V}_1^0\right) + \frac{\mathrm{i}}{k_\mathrm{s}}\boldsymbol{\nabla}\cdot\boldsymbol{v}_1^{d0} \tag{24b}$$

$$\approx \left(V_{1\zeta}^0 - \frac{\mathrm{i}}{k_\mathrm{s}}\boldsymbol{\nabla}_\parallel\cdot\boldsymbol{V}_{1\parallel}^0\right) + \frac{\mathrm{i}}{k_\mathrm{s}}\boldsymbol{\nabla}_\parallel\cdot\boldsymbol{v}_{1\parallel}^{d0}, \tag{24c}$$

where the last step is written for later convenience using $(\mathrm{i}/k_\mathrm{s})\boldsymbol{\nabla}\cdot(\boldsymbol{v}_1^{d0}-\boldsymbol{V}_1^0)=(\mathrm{i}/k_\mathrm{s})\boldsymbol{\nabla}_\parallel\cdot(\boldsymbol{v}_{1\parallel}^{d0}-\boldsymbol{V}_{1\parallel}^0)-(\mathrm{i}\mathcal{H}_\zeta/k_\mathrm{s})v_{1\zeta}^{\delta 0}$ from Eqs. (13a) and (22b) and using that $v_{1\zeta}^{\delta 0}\sim\epsilon|v_1|$. This boundary condition involves the usual expression $V_{1\zeta}^0$ used in classical pressure acoustics plus an $\mathcal{O}(\epsilon)$-correction term proportional to k_s^{-1}, due to the parallel divergence of fluid velocity inside the boundary layer that forces a fluid flow perpendicular to the surface to fulfil the incompressibility of the short-range velocity $\boldsymbol{v}_1^\delta$. Note that this correction term is generated partly by the external wall motion $-(\mathrm{i}/k_\mathrm{s})\boldsymbol{\nabla}_\parallel\cdot\boldsymbol{V}_{1\parallel}^0$ and partly by the fluid motion itself $(\mathrm{i}/k_\mathrm{s})\boldsymbol{\nabla}_\parallel\cdot\boldsymbol{v}_{1\parallel}^{d0}$. Hence, the wall can affect the long-range fields either by a perpendicular component $V_{1\zeta}^0$ or by a parallel divergence $\boldsymbol{\nabla}_\parallel\cdot\boldsymbol{V}_{1\parallel}^0$. The correction term $(\mathrm{i}/k_\mathrm{s})\boldsymbol{\nabla}_\parallel\cdot\boldsymbol{v}_{1\parallel}^{d0}$ due to the fluid motion itself gives the boundary-layer damping of the acoustic energy, see Sec. IV.

Finally, we write Eq. (24b) in terms of the pressure p_1 using $\boldsymbol{\nabla}\cdot\boldsymbol{v}_1^{d0}=\boldsymbol{\nabla}\cdot\boldsymbol{v}_1^d-\partial_\zeta v_{1\zeta}^d$ and Eq. (19),

$$\partial_\zeta p_1=\frac{\mathrm{i}\omega\rho_0}{1-\mathrm{i}\Gamma}\left(V_{1\zeta}^0-\frac{\mathrm{i}}{k_\mathrm{s}}\boldsymbol{\nabla}\cdot\boldsymbol{V}_1^0\right)-\frac{\mathrm{i}}{k_\mathrm{s}}(k_\mathrm{c}^2p_1+\partial_\zeta^2p_1),\quad\text{boundary condition at } \boldsymbol{s}_0. \tag{25}$$

C. Boundary condition for the first-order stress

The boundary condition for the first-order stress $\boldsymbol{\sigma}_1\cdot\boldsymbol{e}_\zeta$ on the surrounding wall is found using Eqs. (2c) and (2d). In the viscous stress $\boldsymbol{\tau}_1$, the divergence terms are neglected, because (19a) leads to $|\eta_0\boldsymbol{\nabla}\cdot\boldsymbol{v}_1^d|\approx\eta_0\omega\kappa_0p_1\approx\Gamma p_1\ll p_1$. The remaining part of $\boldsymbol{\tau}_1$ is dominated by the term $\eta_0\partial_\zeta\boldsymbol{v}_1^\delta$, and we obtain $\boldsymbol{\sigma}_1\cdot\boldsymbol{e}_\zeta=-p_1\boldsymbol{e}_\zeta+\eta_0\partial_\zeta\boldsymbol{v}_1^\delta$ at $\boldsymbol{s}_0$. Here, we insert $\partial_\zeta\boldsymbol{v}_1^\delta=\mathrm{i}k_\mathrm{s}\boldsymbol{v}_1^\delta$ from Eq. (22a), and use Eqs. (19b) and (22b) to express $\boldsymbol{\sigma}_1\cdot\boldsymbol{e}_\zeta$ in terms of the long-range pressure p_1 and wall velocity $\boldsymbol{V}_1^0$ to lowest order in $\Gamma\sim(k_0\delta)^2$,

$$\boldsymbol{\sigma}_1\cdot\boldsymbol{e}_\zeta=-p_1\boldsymbol{e}_\zeta+\mathrm{i}k_\mathrm{s}\eta_0\left(\boldsymbol{V}_1^0+\frac{\mathrm{i}}{\omega\rho_0}\boldsymbol{\nabla}p_1\right),\quad\text{boundary condition at } \boldsymbol{s}_0. \tag{26}$$

This is the usual pressure condition plus a correction term of order ϵ due to the viscous shear stress $\eta_0\partial_\zeta\boldsymbol{v}_1^\delta$ from the boundary layer.

Equations (20), (24), (25), and (26) constitute our main theoretical result for the first-order acoustic fields. Remarkably, explicit reference to the curvilinear quantities are absent in these equations, only the notion of perpendicular and tangential directions and components are important. In the numerical implementation of them in Sec. VII, we use Cartesian coordinates.

IV. ACOUSTIC POWER LOSS

From the pressure p_1, we derive an expression for the acoustic power loss solely in terms of long-range fields. We introduce the energy density E_ac^d and the energy-flux density $\boldsymbol{S}_\mathrm{ac}^d$ of the long-range acoustic fields,

$$E_\mathrm{ac}^d(\boldsymbol{r},t)=\frac{\kappa_0}{2}\left[\mathrm{Re}\left(p_1\mathrm{e}^{-\mathrm{i}\omega t}\right)\right]^2+\frac{\rho_0}{2}\left|\mathrm{Re}\left(\boldsymbol{v}_1^d\mathrm{e}^{-\mathrm{i}\omega t}\right)\right|^2, \tag{27a}$$

$$\boldsymbol{S}_\mathrm{ac}^d(\boldsymbol{r},t)=\mathrm{Re}(p_1\mathrm{e}^{-\mathrm{i}\omega t})\,\mathrm{Re}(\boldsymbol{v}_1^d\mathrm{e}^{-\mathrm{i}\omega t}), \tag{27b}$$

with the time averages

$$\langle E_\mathrm{ac}^d\rangle=\frac{1}{4}\kappa_0|p_1|^2+\frac{1}{4}\rho_0|\boldsymbol{v}_1^d|^2, \tag{28a}$$

$$\langle\boldsymbol{S}_\mathrm{ac}^d\rangle=\langle p_1\boldsymbol{v}_1^d\rangle=c_0^2\langle\rho_1\boldsymbol{v}_1^d\rangle. \tag{28b}$$

In terms of real-valued physical quantities, Eqs. (19a) and (19b) become $\kappa_0\partial_t\mathrm{Re}(p_1\mathrm{e}^{-\mathrm{i}\omega t})=-\boldsymbol{\nabla}\cdot\mathrm{Re}(\boldsymbol{v}_1^d\mathrm{e}^{-\mathrm{i}\omega t})$ and $\rho_0\partial_t\mathrm{Re}(\boldsymbol{v}_1^d\mathrm{e}^{-\mathrm{i}\omega t})=-\boldsymbol{\nabla}\cdot\mathrm{Re}[(1-\mathrm{i}\Gamma)p_1\mathrm{e}^{-\mathrm{i}\omega t}]$. Taking the scalar product of $\mathrm{Re}(\boldsymbol{v}_1^d\mathrm{e}^{-\mathrm{i}\omega t})$ with the latter leads to expressions for the time derivative $\partial_tE_\mathrm{ac}^d$ and its time-averaged value $\langle\partial_tE_\mathrm{ac}^d\rangle$, which is zero due to the harmonic time dependence,

$$\partial_tE_\mathrm{ac}^d=-\boldsymbol{\nabla}\cdot\boldsymbol{S}_\mathrm{ac}^d-\Gamma\rho_0\omega|\mathrm{Re}(\boldsymbol{v}_1^d\mathrm{e}^{-\mathrm{i}\omega t})|^2, \tag{29a}$$

$$-\boldsymbol{\nabla}\cdot\langle\boldsymbol{S}_\mathrm{ac}^d\rangle=\frac{1}{2}\Gamma\omega\rho_0|\boldsymbol{v}_1^d|^2. \tag{29b}$$

The latter expression describes the local balance between the convergence of energy-flux density $\langle\boldsymbol{S}_\mathrm{ac}^d\rangle$ and the rate of change of acoustic energy due to the combined effect of viscous dissipation and viscous energy flux. See Appendix B for a more detailed discussion of this point. Integrating Eq. (29b) over the entire fluid domain Ω, and using Gauss's theorem with the ζ-direction pointing into Ω, leads to the global balance of energy rates,

$$\int_{\partial\Omega}\langle p_1v_{1\zeta}^{d0}\rangle\mathrm{d}A=\int_\Omega\frac{1}{2}\Gamma\rho_0\omega|\boldsymbol{v}_1^d|^2\,\mathrm{d}V. \tag{30}$$

This general result reduces to that of classical pressure acoustics only in the special case where $v_{1\zeta}^{d0}=V_{1\zeta}^0$. As seen from Eq. (24c), $v_{1\zeta}^{d0}$ is generated partly externally by the wall motion, and partly internally by the fluid motion. Inserting Eq. (24c) into Eq. (30), and separating wall-velocity terms from fluid-velocity terms gives

$$\oint_{\partial\Omega}\left\langle p_1\left(V_{1\zeta}^0-\frac{\mathrm{i}}{k_\mathrm{s}}\boldsymbol{\nabla}_\parallel\cdot\boldsymbol{V}_{1\parallel}^0\right)\right\rangle\mathrm{d}A=\int_\Omega\frac{1}{2}\Gamma\rho_0\omega|\boldsymbol{v}_1^d|^2\,\mathrm{d}V-\oint_{\partial\Omega}\left\langle p_1\left(\frac{\mathrm{i}}{k_\mathrm{s}}\boldsymbol{\nabla}_\parallel\cdot\boldsymbol{v}_{1\parallel}^{d0}\right)\right\rangle\mathrm{d}A. \tag{31}$$

Here, the left-hand side represents the acoustic power gain due to the wall motion, while the right-hand side represents the acoustic power loss $\langle P_\mathrm{loss}^d\rangle$ due to the fluid motion. Integrating the last term by parts and using that $\oint_{\partial\Omega}\boldsymbol{\nabla}_\parallel\cdot\langle p_1[(\mathrm{i}/k_\mathrm{s})\boldsymbol{v}_{1\parallel}^{d0}]\rangle\mathrm{d}A=0$ for any closed surface, we can by Eq. (19b) rewrite $\langle P_\mathrm{loss}^d\rangle$ to lowest order in Γ as

$$\frac{1}{\omega}\langle P_\mathrm{loss}^d\rangle=\int_\Omega\frac{\Gamma}{2}\rho_0|\boldsymbol{v}_1^d|^2\,\mathrm{d}V+\oint_{\partial\Omega}\frac{\delta}{4}\rho_0|\boldsymbol{v}_{1\parallel}^{d0}|^2\,\mathrm{d}A, \tag{32}$$

which is always positive. The quality factor Q of an acoustic cavity resonator can be calculated from the long-range fields $\langle E_\mathrm{ac}^d\rangle$ in Eq. (28a) and $\langle P_\mathrm{loss}^d\rangle$ in Eq. (32) as

$$Q = \frac{\int_\Omega \langle E^d_{\mathrm{ac}} \rangle \, \mathrm{d}V}{\frac{1}{\omega} \langle P^d_{\mathrm{loss}} \rangle}, \quad \text{at resonance.} \tag{33}$$

We emphasize that in general, $\langle P_{\mathrm{loss}} \rangle$ is not identical to the viscous heat generation $\langle P^{\mathrm{diss}}_{\mathrm{visc}} \rangle = \int_\Omega \langle \nabla \boldsymbol{v}_1 : \boldsymbol{\tau}_1 \rangle \, \mathrm{d}V$, although as discussed in Appendix B, these might be approximately equal in many common situations.[38]

V. SECOND-ORDER STREAMING FIELDS

As specified in Sec. II B, we only consider the time-averaged streaming and not time-dependent streaming as done by Muller and Bruus.[36] For notational simplicity, we therefore drop the angled bracket $\langle\cdot\rangle$ from the time-averaged velocity $\boldsymbol{v}_2$, pressure p_2, and stress $\boldsymbol{\sigma}_2$. The streaming $\boldsymbol{v}_2$ is governed by the time-averaged part of Eq. (2) to second order in $\mathrm{Ma} = (1/c_0)|\boldsymbol{v}_1|$, together with the boundary condition (8b),

$$0 = \boldsymbol{\nabla} \cdot (\rho_0 \boldsymbol{v}_2 + \langle \rho_1 \boldsymbol{v}_1 \rangle), \quad \text{for } \boldsymbol{r} \in \Omega, \tag{34a}$$

$$\boldsymbol{0} = \boldsymbol{\nabla} \cdot \boldsymbol{\sigma}_2 - \rho_0 \boldsymbol{\nabla} \cdot \langle \boldsymbol{v}_1 \boldsymbol{v}_1 \rangle, \quad \text{for } \boldsymbol{r} \in \Omega, \tag{34b}$$

$$\boldsymbol{0} = \boldsymbol{v}_2 + \langle (\boldsymbol{s}_1 \cdot \boldsymbol{\nabla}) \boldsymbol{v}_1 \rangle, \quad \text{at } \boldsymbol{s}_0. \tag{34c}$$

For the given first-order fields ρ_1 and $\boldsymbol{v}_1$, this is a linear Stokes flow problem for $\boldsymbol{v}_2$ and $\boldsymbol{\sigma}_2$. We decompose the problem into one part driven by the long-range source terms, $\boldsymbol{\nabla} \cdot \langle \rho_1 \boldsymbol{v}^d_1 \rangle$ in Eq. (34a) and $\rho_0 \boldsymbol{\nabla} \cdot \langle \boldsymbol{v}^d_1 \boldsymbol{v}^d_1 \rangle$ in Eq. (34b), and another part driven by the short-range source terms $\boldsymbol{\nabla} \cdot \langle \rho_1 \boldsymbol{v}^\delta_1 \rangle$ and $\rho_0 \boldsymbol{\nabla} \cdot \langle \boldsymbol{v}^\delta_1 \boldsymbol{v}^\delta_1 + \boldsymbol{v}^\delta_1 \boldsymbol{v}^d_1 + \boldsymbol{v}^d_1 \boldsymbol{v}^\delta_1 \rangle$. The corresponding responses are long-range bulk fields "d" and short-range boundary-layer fields "δ,"

$$\boldsymbol{v}_2 = \boldsymbol{v}^d_2 + \boldsymbol{v}^\delta_2, \tag{35a}$$

$$p_2 = p^d_2 + p^\delta_2, \tag{35b}$$

$$\boldsymbol{\sigma}_2 = \boldsymbol{\sigma}^d_2 + \boldsymbol{\sigma}^\delta_2, \tag{35c}$$

$$\boldsymbol{v}^{d0}_2 = -\boldsymbol{v}^{\delta 0}_2 - \langle (\boldsymbol{s}_1 \cdot \boldsymbol{\nabla}) \boldsymbol{v}_1 \rangle, \quad \text{at } \boldsymbol{s}_0. \tag{35d}$$

Given the boundary conditions Eqs. (35d) and (36d), this length-scale-based decomposition of the linear Stokes problem is unique, see Eqs. (36) and (48), but in contrast to the first-order decomposition (18), it is not a Helmholtz decomposition. Nevertheless, the computational strategy remains the same: we find analytical solutions to the short-range δ-fields, and from this we derive boundary conditions for the long-range d-fields.

Note that our method to calculate the steady second-order fields differs from the standard method of matching "inner" boundary-layer solutions with "outer" bulk solutions.[33–35] Our short- and long-range fields co-exist in the boundary layer, but are related by imposing boundary conditions at $\boldsymbol{s}_0$.

A. Short-range boundary-layer streaming

The short-range part of Eq. (34) consists of all terms containing at least one short-range δ-field,

$$0 = \boldsymbol{\nabla} \cdot (\rho_0 \boldsymbol{v}^\delta_2 + \langle \rho_1 \boldsymbol{v}^\delta_1 \rangle), \tag{36a}$$

$$\boldsymbol{0} = -\rho_0 \boldsymbol{\nabla} \cdot \langle \boldsymbol{v}^\delta_1 \boldsymbol{v}^\delta_1 + \boldsymbol{v}^\delta_1 \boldsymbol{v}^d_1 + \boldsymbol{v}^d_1 \boldsymbol{v}^\delta_1 \rangle + \boldsymbol{\nabla} \cdot \boldsymbol{\sigma}^\delta_2, \tag{36b}$$

$$\boldsymbol{\nabla} \cdot \boldsymbol{\sigma}^\delta_2 = \boldsymbol{\nabla}(-p^\delta_2 + \beta \eta_0 \boldsymbol{\nabla} \cdot \boldsymbol{v}^\delta_2) + \eta_0 \nabla^2 \boldsymbol{v}^\delta_2, \tag{36c}$$

$$\text{where } \boldsymbol{v}^\delta_2 \to 0 \text{ as } \zeta \to \infty. \tag{36d}$$

Notably, condition (36d) leads to a nonzero short-range streaming velocity $\boldsymbol{v}^{\delta 0}_2$ at the wall, which, due to the full velocity boundary condition (34c), in turn implies a slip condition $\boldsymbol{v}^{d0}_2$ (35d) on the long-range streaming velocity.

First, we investigate the scaling of p^δ_2 by taking the divergence of Eq. (36b) and using Eqs. (36a) and (36c) together with $\boldsymbol{\nabla} \cdot \boldsymbol{v}^\delta_1 = 0$ and Eq. (19),

$$\begin{aligned} \nabla^2 p^\delta_2 &= -\nu_0 (1+\beta) \nabla^2 \langle \boldsymbol{v}^\delta_1 \cdot \boldsymbol{\nabla} \rho_1 \rangle \\ &\quad - \rho_0 \boldsymbol{\nabla} \cdot \Big(\boldsymbol{\nabla} \cdot \langle \boldsymbol{v}^\delta_1 \boldsymbol{v}^\delta_1 + \boldsymbol{v}^\delta_1 \boldsymbol{v}^d_1 + \boldsymbol{v}^d_1 \boldsymbol{v}^\delta_1 \rangle \Big) \end{aligned} \tag{37a}$$

$$\begin{aligned} &= -\rho_0 \Gamma \nabla^2 \langle \boldsymbol{v}^\delta_1 \cdot (\mathrm{i} \boldsymbol{v}^d_1) \rangle + 2 \rho_0 k_0^2 \langle \boldsymbol{v}^\delta_1 \cdot \boldsymbol{v}^d_1 \rangle \\ &\quad - \rho_0 \Big\langle \boldsymbol{\nabla} (2 \boldsymbol{v}^d_1 + \boldsymbol{v}^\delta_1) \, : \, (\boldsymbol{\nabla} \boldsymbol{v}^\delta_1)^{\mathrm{T}} \Big\rangle. \end{aligned} \tag{37b}$$

Recalling from Eq. (23) that $|v^{\delta 0}_{1\zeta}| \sim \delta d^{-1} v_1$, we find $|\rho_0 (\boldsymbol{\nabla} \boldsymbol{v}^d_1) : (\boldsymbol{\nabla} \boldsymbol{v}^\delta_1)^{\mathrm{T}}| \sim (\delta d)^{-1} \rho_0 v_1^2$ which is the largest possible scaling of the right-hand side. Since by definition p^δ_2 is a boundary-layer field, we have $|\nabla^2 p^\delta_2| \sim \delta^{-2} p^\delta_2$, and the scaling of $|p^\delta_2|$ becomes

$$|p^\delta_2| \lesssim \epsilon \rho_0 v_1^2. \tag{38}$$

Thus, $\boldsymbol{\nabla} p^\delta_2$ can be neglected in the parallel component of Eq. (36b), but not necessarily in the perpendicular one. Similarly, in Eq. (36c) we have $\boldsymbol{\nabla}(\beta \eta_0 \boldsymbol{\nabla} \cdot \boldsymbol{v}^\delta_2) = -\beta \nu_0 \boldsymbol{\nabla} \langle \boldsymbol{v}^\delta_1 \cdot \boldsymbol{\nabla} \rho_1 \rangle$ which scales as $\beta \eta_0 d^{-2} (v_1^2 / c_0)$ and thus much smaller than $|\eta_0 \nabla^2 \boldsymbol{v}^\delta_2| \sim \eta_0 \delta^{-2} (v_1^2 / c_0)$.

Henceforth, using the approximation (15b) for the boundary-layer field $\boldsymbol{v}^\delta_2$ in Eq. (36b), we obtain the parallel equation to lowest order in ϵ,

$$\nu_0 \partial_\zeta^2 \boldsymbol{v}^\delta_{2\parallel} = \Big[\boldsymbol{\nabla} \cdot \langle \boldsymbol{v}^\delta_1 \boldsymbol{v}^d_1 + \boldsymbol{v}^d_1 \boldsymbol{v}^\delta_1 + \boldsymbol{v}^\delta_1 \boldsymbol{v}^\delta_1 \rangle \Big]_\parallel. \tag{39a}$$

Combining this with Eq. (36a), and using Eqs. (15c) and (18), leads to an equation for the perpendicular component $v^{\delta 0}_{2\zeta}$ of the short-range streaming velocity,

$$\partial_\zeta v^{\delta 0}_{2\zeta} = -\boldsymbol{\nabla}_\parallel \cdot \boldsymbol{v}^\delta_{2\parallel} - \frac{1}{\rho_0} \langle \boldsymbol{v}^\delta_1 \cdot \boldsymbol{\nabla} \rho_1 \rangle. \tag{39b}$$

To determine the analytical solution for $\boldsymbol{v}^\delta_{2\parallel}$ in Eq. (39a), we Taylor-expand $\boldsymbol{v}^d_1$ to first order in ζ in the boundary layer, and we use the solution (22a) for $\boldsymbol{v}^\delta_1$,

$$\boldsymbol{v}^d_1 = \boldsymbol{v}^{d0}_1 + (\partial_\zeta \boldsymbol{v}^d_1)^0 \, \zeta, \quad \text{for } \zeta \ll d, \tag{40a}$$

$$\boldsymbol{v}^\delta_1 = \boldsymbol{v}^{\delta 0}_1 \, q(\zeta), \quad \text{with } q(\zeta) = \mathrm{e}^{\mathrm{i} k_s \zeta}. \tag{40b}$$

With these expressions, Eq. (39a) becomes

$$\nu_0\partial_\zeta^2 \boldsymbol{v}_{2\parallel}^{\delta} = \Big\{\boldsymbol{\nabla}\cdot\langle[\boldsymbol{v}_1^{\delta 0}q][\boldsymbol{v}_1^{d0}1] + [\boldsymbol{v}_1^{\delta 0}q][(\partial_\zeta \boldsymbol{v}_1^{d})^0\zeta] + [\boldsymbol{v}_1^{d0}1][\boldsymbol{v}_1^{\delta 0}q] + [(\partial_\zeta \boldsymbol{v}_1^{d})^0\zeta][\boldsymbol{v}_1^{\delta 0}q] + [\boldsymbol{v}_1^{\delta 0}q][\boldsymbol{v}_1^{\delta 0}q]\rangle\Big\}_\parallel. \tag{41}$$

In general, the divergence $\boldsymbol{\nabla}\cdot\langle \boldsymbol{A}_1\boldsymbol{B}_1\rangle$ of the time-averaged outer product of two first-order fields of the form $\boldsymbol{A}_1 = \boldsymbol{A}_1^0(\xi,\eta)\,a(\zeta)$ and $\boldsymbol{B}_1 = \boldsymbol{B}_1^0(\xi,\eta)\,b(\zeta)$, is

$$\boldsymbol{\nabla}\cdot\big\langle[\boldsymbol{A}_1^0 a][\boldsymbol{B}_1^0 b]\big\rangle = \frac{1}{2}\mathrm{Re}\Big\{\boldsymbol{\nabla}\cdot\Big[(\boldsymbol{A}_1^0 a)(\boldsymbol{B}_1^0 b)^*\Big]\Big\} \tag{42a}$$

$$= \frac{1}{2}\mathrm{Re}\big\{\boldsymbol{\nabla}\cdot\big[(ab^*)(\boldsymbol{A}_1^0\boldsymbol{B}_1^{0*})\big]\big\} \tag{42b}$$

$$= \frac{1}{2}\mathrm{Re}\big\{ab^*\boldsymbol{\nabla}\cdot(\boldsymbol{A}_1^0\boldsymbol{B}_1^{0*}) + \boldsymbol{A}_1^0(\boldsymbol{B}_1^{0*}\cdot\boldsymbol{\nabla})(ab^*)\big\} \tag{42c}$$

$$= \frac{1}{2}\mathrm{Re}\Big\{ab^*\boldsymbol{\nabla}\cdot(\boldsymbol{A}_1^0\boldsymbol{B}_1^{0*}) + \boldsymbol{A}_1^0 B_{1\zeta}^{0*}\partial_\zeta(ab^*)\Big\}. \tag{42d}$$

When solving for $\boldsymbol{v}_{2\parallel}^{\delta 0}$ in Eq. (41), we must integrate such divergences twice and then evaluate the result at the surface $\zeta = 0$. The result is

$$\int^{\zeta}\mathrm{d}\zeta_2\int^{\zeta_2}\mathrm{d}\zeta_1\,\boldsymbol{\nabla}\cdot\Big[(\boldsymbol{A}_1^0 a(\zeta_1))(\boldsymbol{B}_1^0 b(\zeta_1))^*\Big]\Big|_{\zeta=0} = \frac{1}{2}\mathrm{Re}\Big\{I_{ab}^{(2)}\boldsymbol{\nabla}\cdot(\boldsymbol{A}_1^0\boldsymbol{B}_1^{0*}) + I_{ab}^{(1)}\boldsymbol{A}_1^0 B_{1\zeta}^{0*}\Big\}, \tag{43a}$$

where we have defined the integrals $I_{ab}^{(n)}$ as

$$I_{ab}^{(1)} = \int^{\zeta}\mathrm{d}\zeta_1\,a(\zeta_1)\,b(\zeta_1)^*|_{\zeta=0}, \tag{43b}$$

$$I_{ab}^{(2)} = \int^{\zeta}\mathrm{d}\zeta_2\int^{\zeta_2}\mathrm{d}\zeta_1\,a(\zeta_1)\,b(\zeta_1)^*|_{\zeta=0}, \tag{43c}$$

$$I_{ab}^{(3)} = \int^{\zeta}\mathrm{d}\zeta_3\int^{\zeta_3}\mathrm{d}\zeta_2\int^{\zeta_2}\mathrm{d}\zeta_1\,a(\zeta_1)\,b(\zeta_1)^*|_{\zeta=0}. \tag{43d}$$

We choose all integration constants to be zero to fulfil the condition (36d) at infinity. From Eq. (41) we see that the functions $a(\zeta)$ and $b(\zeta)$ in our case are either $q(\zeta)$, ζ, or unity. By straightforward integration, we find in increasing order of δ,

$$I_{qq}^{(1)} = -\frac{1}{2}\delta, \quad I_{q1}^{(1)} = -\frac{1+\mathrm{i}}{2}\delta,$$
$$I_{qq}^{(2)} = \frac{1}{4}\delta^2, \quad I_{q1}^{(2)} = \frac{\mathrm{i}}{2}\delta^2, \quad I_{q\zeta}^{(1)} = -\frac{1}{2}\delta^2,$$
$$I_{qq}^{(3)} = -\frac{1}{8}\delta^3, \quad I_{q1}^{(3)} = \frac{1-\mathrm{i}}{4}\delta^3, \quad I_{q\zeta}^{(2)} = -\frac{1-\mathrm{i}}{2}\delta^3. \tag{43e}$$

Using Eq. (43) we find $\boldsymbol{v}_{2\parallel}^{\delta 0}$ by integration of Eq. (41) to leading order in ϵ,

$$\boldsymbol{v}_{2\parallel}^{\delta 0} = \frac{1}{2\nu_0}\mathrm{Re}\Big\{I_{qq}^{(2)}\boldsymbol{\nabla}\cdot\Big(\boldsymbol{v}_1^{\delta 0}\boldsymbol{v}_1^{\delta 0*}\Big) + I_{q1}^{(2)}\boldsymbol{\nabla}\cdot\Big(\boldsymbol{v}_1^{\delta 0}\boldsymbol{v}_1^{d0*}\Big) + I_{1q}^{(2)}\boldsymbol{\nabla}\cdot\Big(\boldsymbol{v}_1^{d0}\boldsymbol{v}_1^{\delta 0*}\Big) + I_{qq}^{(1)}\boldsymbol{v}_1^{\delta 0}v_{1\zeta}^{\delta 0*} + I_{1q}^{(1)}\boldsymbol{v}_1^{d0}v_{1\zeta}^{\delta 0*} + I_{q1}^{(1)}\boldsymbol{v}_1^{\delta 0}v_{1\zeta}^{d0*} + I_{q\zeta}^{(1)}\boldsymbol{v}_1^{\delta 0}\partial_\zeta v_{1\zeta}^{d*}\Big\}_\parallel. \tag{44}$$

We have neglected the term $(1/2\nu_0)\mathrm{Re}\{I_{\zeta q}^{(1)}(\partial_\zeta \boldsymbol{v}_1^d)^0 v_{1\zeta}^{\delta 0*}\}$, as $v_{1\zeta}^{\delta 0} \sim \epsilon|\boldsymbol{v}_{1\parallel}^{\delta 0}|$ due to Eq. (23), and the two terms proportional to $I_{\zeta q}^{(2)}$ and $I_{q\zeta}^{(2)}$, as these are $\sim\delta^3$. Remarkably, the term $I_{q1}^{(1)}\boldsymbol{v}_1^{\delta 0}v_{1\zeta}^{d0*}$ may scale with an extra factor ϵ^{-1} compared to all other terms, and thus may dominate the boundary-layer velocity. However, in the computation of the long-range slip velocity $\boldsymbol{v}_{2\parallel}^{d0}$ in Sec. V B, its contribution is canceled by the Stokes drift $\langle \boldsymbol{s}_1\cdot\boldsymbol{\nabla}\boldsymbol{v}_1\rangle$, as also noted in Ref. 35. Using $\boldsymbol{v}_1^{d0} = \boldsymbol{V}_1^0 - \boldsymbol{v}_1^{\delta 0}$, the property $(I_{ab}^{(n)})^* = I_{ba}^{(n)}$, and rearranging terms, we arrive at

$$\boldsymbol{v}_{2\parallel}^{\delta 0} = \frac{1}{2\nu_0}\mathrm{Re}\Big\{\Big(I_{qq}^{(2)} - 2\mathrm{Re}I_{q1}^{(2)}\Big)\boldsymbol{\nabla}\cdot\Big(\boldsymbol{v}_1^{\delta 0}\boldsymbol{v}_1^{\delta 0*}\Big) + I_{q1}^{(2)}\boldsymbol{\nabla}\cdot\Big(\boldsymbol{v}_1^{\delta 0}\boldsymbol{V}_1^{0*}\Big) + I_{1q}^{(2)}\boldsymbol{\nabla}\cdot\Big(\boldsymbol{V}_1^{0}\boldsymbol{v}_1^{\delta 0*}\Big) + \Big(I_{qq}^{(1)} - 2\mathrm{Re}I_{q1}^{(1)}\Big)\boldsymbol{v}_1^{\delta 0}v_{1\zeta}^{\delta 0*} + I_{1q}^{(1)}\boldsymbol{V}_1^0 v_{1\zeta}^{\delta 0*} + I_{q1}^{(1)}\boldsymbol{v}_1^{\delta 0}V_{1\zeta}^{0*} + I_{q\zeta}^{(1)}\boldsymbol{v}_1^{\delta 0}\partial_\zeta v_{1\zeta}^{d*}\Big\}_\parallel. \tag{45}$$

The perpendicular short-range velocity component $v_{2\zeta}^{\delta 0}$ is found by integrating Eq. (39b) with respect to ζ. The integration of the $\boldsymbol{\nabla}_\parallel\cdot\boldsymbol{v}_{2\parallel}^{\delta}$-term is carried out by simply increasing the superscript of the $I_{ab}^{(n)}$-integrals in Eq. (45) from "(n)" to "$(n+1)$," while the integration of the $\boldsymbol{\nabla}\rho_1$-term is carried out by using Eq. (19b) to substitute $(1/\rho_0)\boldsymbol{\nabla}\rho_1$ by $\mathrm{i}\omega c_0^{-2}\,\boldsymbol{v}_1^d$ and introducing the suitable $I_{ab}^{(n)}$-integral for the factor $q(\zeta)\,\mathrm{i}$, namely, $I_{q\mathrm{i}}^{(1)} = -\mathrm{i}I_{q1}^{(1)}$,

$$v_{2\zeta}^{\delta 0} = -\frac{1}{2\nu_0}\boldsymbol{\nabla}_\parallel\cdot\mathrm{Re}\Big\{\Big(I_{qq}^{(3)} - 2\mathrm{Re}I_{q1}^{(3)}\Big)\boldsymbol{\nabla}\cdot\Big(\boldsymbol{v}_1^{\delta 0}\boldsymbol{v}_1^{\delta 0*}\Big) + I_{q1}^{(3)}\boldsymbol{\nabla}\cdot\Big(\boldsymbol{v}_1^{\delta 0}\boldsymbol{V}_1^{0*}\Big) + I_{1q}^{(3)}\boldsymbol{\nabla}\cdot\Big(\boldsymbol{V}_1^{0}\boldsymbol{v}_1^{\delta 0*}\Big) + \Big(I_{qq}^{(2)} - 2\mathrm{Re}I_{q1}^{(2)}\Big)\boldsymbol{v}_1^{\delta 0}v_{1\zeta}^{\delta 0*} + I_{1q}^{(2)}\boldsymbol{V}_1^0 v_{1\zeta}^{\delta 0*} + I_{q1}^{(2)}\boldsymbol{v}_1^{\delta 0}V_{1\zeta}^{0*} + I_{q\zeta}^{(2)}\boldsymbol{v}_1^{\delta 0}\partial_\zeta v_{1\zeta}^{d*}\Big\}_\parallel + \frac{k_0}{2c_0}\mathrm{Re}\Big\{\mathrm{i}I_{q1}^{(1)}\boldsymbol{v}_1^{\delta 0}\cdot\boldsymbol{v}_1^{d0*}\Big\}. \tag{46}$$

Using Eq. (43e), expressions (45) and (46) for the short-range streaming at the surface $\zeta = 0$ become

$$\boldsymbol{v}_{2\parallel}^{\delta 0} = \frac{1}{2\omega}\mathrm{Re}\Big\{\frac{1}{2}\boldsymbol{\nabla}\cdot\Big(\boldsymbol{v}_1^{\delta 0}\boldsymbol{v}_1^{\delta 0*}\Big) + \mathrm{i}\boldsymbol{\nabla}\cdot\Big(\boldsymbol{v}_1^{\delta 0}\boldsymbol{V}_1^{0*}\Big) - \mathrm{i}\boldsymbol{\nabla}\cdot\Big(\boldsymbol{V}_1^{0}\boldsymbol{v}_1^{\delta 0*}\Big) + \frac{1}{\delta}\boldsymbol{v}_1^{\delta 0}v_{1\zeta}^{\delta 0*} - \mathrm{i}\boldsymbol{v}_1^{\delta 0}\partial_\zeta v_{1\zeta}^{d*} - \frac{1-\mathrm{i}}{\delta}\boldsymbol{V}_1^0 v_{1\zeta}^{\delta 0*} - \frac{1+\mathrm{i}}{\delta}\boldsymbol{v}_1^{\delta 0}V_{1\zeta}^{0*}\Big\}_\parallel \tag{47a}$$

and

$$v_{2\zeta}^{\delta 0} = -\frac{\delta}{2\omega}\mathrm{Re}\Big[\boldsymbol{\nabla}_\parallel\cdot\Big\{-\frac{5}{4}\boldsymbol{\nabla}\cdot\Big(\boldsymbol{v}_1^{\delta 0}\boldsymbol{v}_1^{\delta 0*}\Big) + \frac{1-\mathrm{i}}{2}\boldsymbol{\nabla}\cdot\Big(\boldsymbol{v}_1^{\delta 0}\boldsymbol{V}_1^{0*}\Big) + \frac{1+\mathrm{i}}{2}\boldsymbol{\nabla}\cdot\Big(\boldsymbol{V}_1^{0}\boldsymbol{v}_1^{\delta 0*}\Big) + \frac{1}{2\delta}\boldsymbol{v}_1^{\delta 0}v_{1\zeta}^{\delta 0*} - \frac{\mathrm{i}}{\delta}\boldsymbol{V}_1^0 v_{1\zeta}^{\delta 0*} + \frac{\mathrm{i}}{\delta}\boldsymbol{v}_1^{\delta 0}V_{1\zeta}^{0*} - (1-\mathrm{i})\boldsymbol{v}_1^{\delta 0}\partial_\zeta v_{1\zeta}^{d*}\Big\}_\parallel - k_0^2(1-\mathrm{i})\boldsymbol{v}_1^{\delta 0}\cdot\boldsymbol{v}_1^{d0*}\Big] \tag{47b}$$

$$= -\frac{1}{2\omega}\mathrm{Re}\Big[\boldsymbol{\nabla}_\parallel\cdot\Big(\mathrm{i}\boldsymbol{v}_{1\parallel}^{\delta 0}V_{1\zeta}^{0*}\Big)\Big] + \mathcal{O}(\epsilon). \tag{47c}$$

B. Long-range bulk streaming

The long-range part of Eq. (34) is

$$0 = \boldsymbol{\nabla}\cdot\big[\rho_0\boldsymbol{v}_2^d + \langle\rho_1\boldsymbol{v}_1^d\rangle\big], \tag{48a}$$

$$\boldsymbol{0} = -\rho_0\boldsymbol{\nabla}\cdot\langle\boldsymbol{v}_1^d\boldsymbol{v}_1^d\rangle + \boldsymbol{\nabla}\cdot\boldsymbol{\sigma}_2^d, \tag{48b}$$

$$\boldsymbol{\nabla}\cdot\boldsymbol{\sigma}_2^d = -\boldsymbol{\nabla}(p_2^d - \beta\eta_0\boldsymbol{\nabla}\cdot\boldsymbol{v}_2^d) + \eta_0\nabla^2\boldsymbol{v}_2^d, \tag{48c}$$

$$\boldsymbol{v}_2^{d0} = -\boldsymbol{v}_2^{\delta 0} - \langle(\boldsymbol{s}_1\cdot\boldsymbol{\nabla})\boldsymbol{v}_1\rangle, \text{ at } \boldsymbol{s}_0. \tag{48d}$$

In contrast to the limiting-velocity matching at the outer edge of the boundary layer done by Nyborg,[33] we define the boundary condition (48d) on the long-range streaming $\boldsymbol{v}_2^d$ at the equilibrium position $\boldsymbol{s}_0$.

To simplify Eq. (48), we investigate the products of first-order fields. In Eq. (48a), we use Eq. (29b) and find

$$\boldsymbol{\nabla}\cdot\boldsymbol{v}_2^d = -\frac{\boldsymbol{\nabla}\cdot\langle\rho_1\boldsymbol{v}_1^d\rangle}{\rho_0} = -\frac{\boldsymbol{\nabla}\cdot\langle\boldsymbol{S}_{\mathrm{ac}}^d\rangle}{\rho_0 c_0^2} = \Gamma\frac{k_0|\boldsymbol{v}_1^d|^2}{2c_0}. \tag{49}$$

Since each term in $\boldsymbol{\nabla}\cdot\boldsymbol{v}_2^d$ scales as $(k_0/c_0)|\boldsymbol{v}_1^d|^2 \gg (\Gamma/2)(k_0/c_0)\,|\boldsymbol{v}_1^d|^2$, we conclude that $\boldsymbol{\nabla}\cdot\boldsymbol{v}_2^d \approx 0$ is a good approximation, corresponding to ignoring the small viscous dissipation in the energy balance expressed by Eq. (29b). In Eq. (48b), the divergence of momentum flux can be rewritten using Eq. (19b),

$$\rho_0\boldsymbol{\nabla}\cdot\langle\boldsymbol{v}_1^d\boldsymbol{v}_1^d\rangle = -\boldsymbol{\nabla}\langle\mathcal{L}_{\mathrm{ac}}^d\rangle - \frac{\Gamma\omega}{c_0^2}\langle\boldsymbol{S}_{\mathrm{ac}}^d\rangle, \tag{50}$$

where we introduced the long-range time-averaged acoustic Lagrangian density,

$$\langle\mathcal{L}_{\mathrm{ac}}^d\rangle = \frac{1}{4}\kappa_0|p_1|^2 - \frac{1}{4}\rho_0|\boldsymbol{v}_1^d|^2. \tag{51}$$

Note that $|\boldsymbol{\nabla}\langle\mathcal{L}_{\mathrm{ac}}^d\rangle| \sim \omega p_1^2/\rho_0 c_0^3$, whereas $|(\Gamma\omega/c_0^2)\langle\boldsymbol{S}_{\mathrm{ac}}^d\rangle| \sim \Gamma\omega p_1^2/(\rho_0 c_0^3)$, so the first term in Eq. (50) is much larger than the second term. However, as also noted by Riaud *et al.*,[39] since the first term is a gradient, it cannot drive any rotating streaming. In practice, it is therefore advantageous to work with the excess pressure $p_2^d - \langle\mathcal{L}_{\mathrm{ac}}^d\rangle$. Finally, in Eq. (48c), we again use $\boldsymbol{\nabla}\cdot\boldsymbol{v}_2^d \approx 0$. With these considerations, Eqs. (48) become those of an incompressible Stokes flow driven by the body force $(\Gamma\omega/c_0^2)\langle\boldsymbol{S}_{\mathrm{ac}}^d\rangle$ and the slip velocity $\boldsymbol{v}_2^{d0}$ at the boundary,

$$0 = \boldsymbol{\nabla}\cdot\boldsymbol{v}_2^d, \tag{52a}$$

$$\boldsymbol{0} = -\boldsymbol{\nabla}\Big[p_2^d - \big\langle\mathcal{L}_{\mathrm{ac}}^d\big\rangle\Big] + \eta_0\nabla^2\boldsymbol{v}_2^d + \frac{\Gamma\omega}{c_0^2}\big\langle\boldsymbol{S}_{\mathrm{ac}}^d\big\rangle, \tag{52b}$$

$$\boldsymbol{v}_2^{d0} = -\boldsymbol{v}_2^{\delta 0} - \langle(\boldsymbol{s}_1\cdot\boldsymbol{\nabla})\boldsymbol{v}_1\rangle|_{\zeta=0}. \tag{52c}$$

These equations describe acoustic streaming in general. The classical Eckart streaming[40] originates from the body force $(\Gamma\omega/c_0^2)\langle\boldsymbol{S}_{\mathrm{ac}}^d\rangle$, while the classical Rayleigh streaming[22] is due to the boundary condition (52c).

The Stokes drift $\langle\boldsymbol{s}_1\cdot\boldsymbol{\nabla}\boldsymbol{v}_1\rangle|_{\zeta=0}$, induced by the oscillating wall, is computed from Eqs. (6), (18), and (22a),

$$\begin{aligned}\langle\boldsymbol{s}_1\cdot\boldsymbol{\nabla}\boldsymbol{v}_1\rangle|_{\zeta=0} &= -\frac{1}{2\omega}\mathrm{Re}\Big[\mathrm{i}\boldsymbol{V}_1^{0*}\cdot\boldsymbol{\nabla}\Big(\boldsymbol{v}_1^d + \boldsymbol{v}_1^{\delta 0}q\Big)\Big]_{\zeta=0}\\ &= -\frac{1}{2\omega}\mathrm{Re}\Big[\mathrm{i}\boldsymbol{V}_1^{0*}\cdot\boldsymbol{\nabla}\Big(\boldsymbol{v}_1^d + \boldsymbol{v}_1^{\delta 0}\Big) - \frac{1+\mathrm{i}}{\delta}V_{1\zeta}^{0*}\boldsymbol{v}_1^{\delta 0}\Big].\end{aligned} \tag{53}$$

From this, combined with Eqs. (47) and (52c), follows the boundary condition $\boldsymbol{v}_2^{d0}$ for the long-range streaming velocity $\boldsymbol{v}_2^d$ expressed in terms of the short-range velocity $\boldsymbol{v}_2^{\delta 0}$ and the wall velocity $\boldsymbol{V}_1^0$. The parallel component is

$$\boldsymbol{v}_{2\parallel}^{d0} = -\frac{1}{2\omega}\mathrm{Re}\Big\{\boldsymbol{\nabla}\cdot\Big(\frac{1}{2}\boldsymbol{v}_1^{\delta 0}\boldsymbol{v}_1^{\delta 0*} + \mathrm{i}\boldsymbol{v}_1^{\delta 0}\boldsymbol{V}_1^{0*} - \mathrm{i}\boldsymbol{V}_1^0\boldsymbol{v}_1^{\delta 0*}\Big) + \frac{1}{\delta}\boldsymbol{v}_1^{\delta 0}v_{1\zeta}^{\delta 0*} - \mathrm{i}\boldsymbol{v}_1^{\delta 0}\partial_\zeta v_{1\zeta}^{d*} - \frac{1-\mathrm{i}}{\delta}\boldsymbol{V}_1^0 v_{1\zeta}^{\delta 0*} - \mathrm{i}\boldsymbol{V}_1^{0*}\cdot\boldsymbol{\nabla}\Big(\boldsymbol{v}_1^d + \boldsymbol{v}_1^{\delta 0}\Big)\Big\}_\parallel, \tag{54a}$$

where the large terms proportional to $[(1+\mathrm{i})/\delta]V_{1\zeta}^{0*}\boldsymbol{v}_{1\parallel}^{\delta 0}$ canceled out, as also noted by Vanneste and Bühler.[35] Similarly, the perpendicular component becomes

$$\begin{aligned}v_{2\zeta}^{d0} &= \frac{\delta}{2\omega}\mathrm{Re}\Big[-k_0^2(1-\mathrm{i})\boldsymbol{v}_1^{\delta 0}\cdot\boldsymbol{v}_1^{d0*} + \boldsymbol{\nabla}_\parallel\\ &\quad\cdot\Big\{\boldsymbol{\nabla}\cdot\Big[-\frac{5}{4}\boldsymbol{v}_1^{\delta 0}\boldsymbol{v}_1^{\delta 0*} + \frac{1+\mathrm{i}}{2}\Big(\boldsymbol{V}_1^0\boldsymbol{v}_1^{\delta 0*} + \boldsymbol{v}_1^{\delta 0*}\boldsymbol{V}_1^0\Big)\Big]\\ &\quad + \Big[\frac{1}{2\delta}v_{1\zeta}^{\delta 0*} + \frac{\mathrm{i}}{\delta}V_{1\zeta}^{0*} - (1-\mathrm{i})\partial_\zeta v_{1\zeta}^{d*}\Big]\boldsymbol{v}_1^{\delta 0}\\ &\quad - \frac{\mathrm{i}}{\delta}v_{1\zeta}^{\delta 0*}\boldsymbol{V}_1^0\Big\}_\parallel\Big] + \frac{1}{2\omega}\mathrm{Re}\Big[\mathrm{i}\boldsymbol{V}_1^{0*}\cdot\boldsymbol{\nabla}\Big(\boldsymbol{v}_1^d + \boldsymbol{v}_1^{\delta 0}\Big)\\ &\quad - \frac{1+\mathrm{i}}{\delta}V_{1\zeta}^{0*}\boldsymbol{v}_1^{\delta 0}\Big]_\zeta\end{aligned} \tag{54b}$$

$$= \frac{1}{2\omega}\mathrm{Re}\Big[\boldsymbol{\nabla}_\parallel\cdot\Big(\mathrm{i}\boldsymbol{v}_{1\parallel}^{\delta 0}V_{1\zeta}^{0*}\Big) - \frac{1+\mathrm{i}}{\delta}V_{1\zeta}^{0*}v_{1\zeta}^{\delta 0} + \Big\{\mathrm{i}\boldsymbol{V}_1^{0*}\cdot\boldsymbol{\nabla}\Big(\boldsymbol{v}_1^d + \boldsymbol{v}_1^{\delta 0}\Big)\Big\}_\zeta\Big] + \mathcal{O}(\epsilon). \tag{54c}$$

Taking the divergences in Eq. (54a) and using Eq. (23), as well as computing Eq. (54c) to lowest order in ϵ, leads to the final expression for the slip velocity at $\zeta = 0$,

$$\begin{aligned}
\boldsymbol{v}_2^{d0} &= (\boldsymbol{A}\cdot\boldsymbol{e}_\xi)\boldsymbol{e}_\xi + (\boldsymbol{A}\cdot\boldsymbol{e}_\eta)\boldsymbol{e}_\eta + (\boldsymbol{B}\cdot\boldsymbol{e}_\zeta)\boldsymbol{e}_\zeta,\\
\boldsymbol{A} &= -\frac{1}{2\omega}\mathrm{Re}\Big\{\boldsymbol{v}_1^{\delta 0*}\cdot\nabla\Big(\frac{1}{2}\boldsymbol{v}_1^{\delta 0} - \mathrm{i}\boldsymbol{V}_1^0\Big) - \mathrm{i}\boldsymbol{V}_1^{0*}\cdot\nabla\boldsymbol{v}_1^d\\
&\quad + \Big[\frac{2-\mathrm{i}}{2}\nabla\cdot\boldsymbol{v}_1^{\delta 0*} + \mathrm{i}\Big(\nabla\cdot\boldsymbol{V}_1^{0*} - \partial_\zeta v_{1\zeta}^{d*}\Big)\Big]\boldsymbol{v}_1^{\delta 0}\Big\},\\
\boldsymbol{B} &= \frac{1}{2\omega}\mathrm{Re}\big\{\mathrm{i}\boldsymbol{v}_1^{d0*}\cdot\nabla\boldsymbol{v}_1^d\big\},
\end{aligned} \tag{55}$$

where $\boldsymbol{A}$ and $\boldsymbol{B}$ are associated with the parallel and perpendicular components $\boldsymbol{v}_{2\|}^{d0}$ and $\boldsymbol{v}_{2\zeta}^{d0}$, respectively, and where to simplify we used $(\boldsymbol{v}_{1\|}^{\delta 0}\cdot\nabla_\|)V_{1\zeta}^{0*} = (\boldsymbol{v}_1^{\delta 0}\cdot\nabla)V_{1\zeta}^{0*}$ and the relations $T_{\zeta ji} = 0$, $T_{kjj} = 0$, and $T_{kji} = T_{jki}$ for the curvilinear quantities, see Eq. (A3) in Appendix A.

Equations (52) and (55) constitute our main theoretical result for the second-order acoustic streaming.

VI. SPECIAL CASES

In the following, we study some special cases of our main results (20a) and (25) for the acoustic pressure p_1 and Eqs. (52) and (55) for the streaming velocity $\boldsymbol{v}_2^d$, and relate them to previous studies in the literature.

A. Wall oscillations restricted to the perpendicular direction

The case of a weakly curved wall oscillating only in the perpendicular direction was studied by Nyborg[33] and later refined by Lee and Wang.[34] Using our notation, the boundary conditions used in these studies were

$$\boldsymbol{v}_1^{d0} + \boldsymbol{v}_1^{\delta 0} = \boldsymbol{V}_1^0 = V_{1\zeta}^0\,\boldsymbol{e}_\zeta, \tag{56}$$

whereby $\nabla\cdot\boldsymbol{V}_1^0 = \mathcal{H}_\zeta V_{1\zeta}^0$, so that our boundary condition (25) for p_1 to lowest order in Γ becomes

$$\partial_\zeta p_1 = \mathrm{i}\omega\rho_0\Big(1 - \frac{\mathrm{i}}{k_\mathrm{s}}\mathcal{H}_\zeta\Big)V_{1\zeta}^0 - \frac{\mathrm{i}}{k_\mathrm{s}}\Big(k_\mathrm{c}^2 p_1 + \partial_\zeta^2 p_1\Big). \tag{57}$$

Similarly, for the steady streaming $\boldsymbol{v}_2^d$, Eq. (56) gives $\nabla\cdot\boldsymbol{v}_1^{\delta 0} \approx -\nabla_\|\cdot\boldsymbol{v}_{1\|}^{d0} = -(\nabla\cdot\boldsymbol{v}_1^d - \partial_\zeta v_{1\zeta}^d - \mathcal{H}_\zeta V_{1\zeta}^0)$ evaluated at $\zeta = 0$. Combining this expression with the derivative rule (13b) and the index notation $\bar{\xi} = \eta$ and $\bar{\eta} = \xi$, as well as $\alpha, \beta = \xi, \eta$, the boundary condition (55) gives to lowest order in ϵ the tangential components

$$\begin{aligned}
v_{2\beta}^{d0} &= -\frac{1}{4\omega}\mathrm{Re}\Big\{v_{1\alpha}^{d0*}\Big(\tilde{\partial}_\alpha v_{1\beta}^{d0}\Big) + v_{1\alpha}^{d0*}v_{1\bar{\beta}}^{d0}T_{\alpha\bar{\beta}\beta}\\
&\quad + 2\mathrm{i}V_{1\zeta}^0\Big(\partial_\zeta v_{1\beta}^{d*} + v_{1\alpha}^{d0*}T_{\alpha\zeta\beta}\Big) + \Big[(2-\mathrm{i})\nabla\cdot\boldsymbol{v}_1^{d*}\\
&\quad -(2-3\mathrm{i})\partial_\zeta v_{1\zeta}^{d*} - (2+\mathrm{i})\mathcal{H}_\zeta V_{1\zeta}^{0*}\Big]v_{1\beta}^d\Big\}.
\end{aligned} \tag{58a}$$

and the perpendicular component

$$v_{2\zeta}^{d0} = \frac{1}{2\omega}\mathrm{Re}\Big\{\mathrm{i}v_{1k}^{d0*}\,\tilde{\partial}_k v_{1\zeta}^d\Big\}. \tag{58b}$$

When comparing our expressions with the results of Lee and Wang,[34] denoted by a superscript "LW" below, we note the following. Neither the pressure p_1 nor the steady perpendicular streaming velocity $v_{2\zeta}^d$ were studied by Lee and Wang, so our results Eqs. (57) and (58b) for these fields represent an extension of their work. The slip condition (58a) for the parallel streaming velocity $v_{2\beta}^d$ with $\beta = \xi, \eta$ is presented in Eqs. $(19)^{\mathrm{LW}}$ and $(20)^{\mathrm{LW}}$ as the limiting values u_L and v_L for the two parallel components of $\boldsymbol{v}_2^d$ outside the boundary layer. A direct comparison is obtained by (1) identifying our $\boldsymbol{v}_1^d$ with the acoustic velocity $(u_{a0}, v_{a0}, w_{a0})^{\mathrm{LW}}$, and our T_{kji} with T_{ijk}^{LW}; (2) taking the complex conjugate of the argument of the real value in Eq. (58a), and (3) noting that q_x and q_y defined in Eqs. $(3)^{\mathrm{LW}}$ and $(4)^{\mathrm{LW}}$ equal the first two terms of Eq. (58a). By inspection we find agreement, except that Lee and Wang are missing the terms $2\mathrm{i}V_{1\zeta}^0(\partial_\zeta v_{1\beta}^{d*} + v_{1\alpha}^{d0*}T_{\alpha\zeta\beta})$, which in our calculation partly arise from the Lagrangian velocity boundary condition (34c), where Lee and Wang have used the no slip condition $\boldsymbol{v}_2 = \boldsymbol{0}$. For more details see Appendix C 1.

B. A flat wall oscillating in any direction

The case of a flat wall oscillating in any direction was studied by Vanneste and Bühler.[35] In this case, we adapt Cartesian coordinates $(\xi, \eta, \zeta) = (x, y, z)$, for which all scale factors h_i are unity, $\tilde{\partial}_i = \partial_i$, and all curvilinear quantities T_{kji} and $\mathcal{H}_k$ are zero. The resulting boundary conditions (25) and (55) for the pressure p_1 and for the long-range streaming $\boldsymbol{v}_2^d$, then simplify to

$$\partial_\zeta p_1 = \mathrm{i}\omega\rho_0 V_{1\zeta}^0 - \frac{1+\mathrm{i}}{2}\delta\Big(\mathrm{i}\omega\rho_0\nabla_\|\cdot\boldsymbol{V}_{1\|}^0 + k_\mathrm{c}^2 p_1 + \partial_\zeta^2 p_1\Big), \tag{59a}$$

$$\begin{aligned}
v_{2\beta}^{d0} &= -\frac{1}{4\omega}\mathrm{Re}\Big\{(1-2\mathrm{i})v_{1\alpha}^{\delta 0*}\partial_\alpha v_{1\beta}^{\delta 0} - 4\mathrm{i}v_{1\alpha}^{\delta 0*}\partial_\alpha v_{1\beta}^{d0}\\
&\quad + \Big[(2+\mathrm{i})\partial_\alpha v_{1\alpha}^{\delta 0*} + 2\mathrm{i}\Big(\partial_\alpha v_{1\alpha}^{d0*} - \partial_\zeta v_{1\zeta}^{d*}\Big)\Big]\\
&\quad \times v_{1\beta}^{\delta 0} - 2\mathrm{i}\,v_{1k}^{d*}\partial_k v_{1\beta}^d\Big\},
\end{aligned} \tag{59b}$$

$$v_{2\zeta}^{d0} = -\frac{1}{4\omega}\mathrm{Re}\Big\{-2\mathrm{i}\,v_{1k}^{d*}\partial_k v_{1\zeta}^d\Big\}. \tag{59c}$$

The pressure condition (59a) was not studied in Ref. 35, so it represents an extension of the existing theory. On the other hand, Eqs. (59b) and (59c) are in full agreement with Eq. (4.14) in Vanneste and Bühler.[35] To see this, we identify our first-order symbols with those used in Ref. 35 as $\boldsymbol{v}_1^d = 2\nabla\hat{\phi}$ and $\boldsymbol{v}_{1\|}^{\delta 0} = -2\hat{U}\boldsymbol{e}_x - 2\hat{V}\boldsymbol{e}_y$, and we relate our steady Eulerian second-order long-range velocity $\boldsymbol{v}_2^d$ with their Lagrangian mean flow $\bar{\boldsymbol{u}}^{\mathrm{L}}$ using the Stokes drift expression (34c) as $\boldsymbol{v}_2^d + (1/\omega)\langle\mathrm{i}\boldsymbol{v}_1^d\cdot\nabla\boldsymbol{v}_1^d\rangle = \bar{\boldsymbol{u}}^{\mathrm{L}}$ at the interface $z = 0$. For more details see Appendix C 2.

C. Small surface velocity compared to the bulk velocity

At resonance in acoustic devices with a large resonator quality factor $Q \gg 1$, the wall velocity $\boldsymbol{V}_1^0$ is typically a

factor Q smaller than the bulk fluid velocity $\boldsymbol{v}_1^d$,[25,36] which is written as $V_1^0 \sim Q^{-1} v_1^d \ll v_1^d$. In this case, as well as for rigid walls, we use $\boldsymbol{V}_1^0 = \boldsymbol{0}$ in Eq. (55), so that $\boldsymbol{v}_1^{\delta 0} = -\boldsymbol{v}_1^{d0}$ and

$$\left\langle \boldsymbol{v}_1^{\delta 0} \cdot \boldsymbol{\nabla} \boldsymbol{v}_1^{\delta 0} \right\rangle = \left\langle \boldsymbol{v}_1^{d0} \cdot \boldsymbol{\nabla} \boldsymbol{v}_1^{d0} \right\rangle \approx \frac{1}{4} \boldsymbol{\nabla}_\parallel |\boldsymbol{v}_{1\parallel}^{d0}|^2. \tag{60}$$

Here, $v_{1\zeta}^{d0}$ is neglected because $|v_{1\zeta}^{d0}| \approx |V_{1\zeta}^0| \ll |\boldsymbol{v}_{1\parallel}^{d0}|$, and we have used that $\boldsymbol{\nabla} \times \boldsymbol{v}_1^d = 0$ from Eq. (18). Hence, for devices with rigid walls $\boldsymbol{V}_1^0 = \boldsymbol{0}$, or resonant devices with $|\boldsymbol{v}_1^{d0}| \gg |\boldsymbol{V}_1^0|$, the slip-velocity $\boldsymbol{v}_2^{d0}$ becomes

$$\boldsymbol{v}_{2\parallel}^{d0} = \frac{-1}{8\omega} \boldsymbol{\nabla}_\parallel |\boldsymbol{v}_{1\parallel}^{d0}|^2 - \mathrm{Re}\left\{ \left(\frac{2-\mathrm{i}}{4\omega} \boldsymbol{\nabla}_\parallel \cdot \boldsymbol{v}_{1\parallel}^{d0*} + \frac{\mathrm{i}}{2\omega} \partial_\zeta v_{1\zeta}^{d*} \right) \boldsymbol{v}_{1\parallel}^{d0} \right\}, \tag{61a}$$

$$v_{2\zeta}^{d0} = 0. \tag{61b}$$

Two important limits are parallel acoustics, where $|\partial_\zeta v_{1\zeta}^d| \ll |\boldsymbol{\nabla}_\parallel \cdot \boldsymbol{v}_{1\parallel}^{d0}|$, and perpendicular acoustics, where $|\partial_\zeta v_{1\zeta}^d| \gg |\boldsymbol{\nabla}_\parallel \cdot \boldsymbol{v}_{1\parallel}^{d0}|$. In the first limit, the pressure is mainly related to the parallel velocity variations, and from Eqs. (19a) and (19b) we have $\boldsymbol{\nabla}_\parallel \cdot \boldsymbol{v}_{1\parallel}^{d0} = \mathrm{i}\omega\kappa_0 p_1$ and $\boldsymbol{v}_{1\parallel}^{d0} = -(\mathrm{i}/\rho_0\omega)\boldsymbol{\nabla}_\parallel p_1$. For parallel acoustics we can therefore write Eq. (61a) as,

$$\boldsymbol{v}_{2\parallel}^{d0} = \frac{1}{8\omega\rho_0} \boldsymbol{\nabla}_\parallel \left(2\kappa_0 |p_1|^2 - \rho_0 |\boldsymbol{v}_{1\parallel}^{d0}|^2 \right) + \frac{\kappa_0}{2} \langle \boldsymbol{S}_{\mathrm{ac}\parallel}^d \rangle, \quad \text{for parallel acoustics, } |\partial_\zeta v_{1\zeta}^d| \ll |\boldsymbol{\nabla}_\parallel \cdot \boldsymbol{v}_{1\parallel}^{d0}|. \tag{62a}$$

The classical period-doubled Rayleigh streaming,[22] which arises from a one-dimensional parallel standing wave, results from the gradient-term in Eq. (62a). This is seen by considering a rigid wall in the x-y plane with a standing wave above it in the x direction of the form $\boldsymbol{v}_1^d = v_{1a}\cos(k_0 x)\,\boldsymbol{e}_x$, where v_{1a} is a velocity amplitude. Inserting this into Eq. (62a) yields Rayleigh's seminal boundary velocity $\boldsymbol{v}_{2\parallel}^{d0} = (3/8)(v_{1a}^2/c_0)\sin(2k_0 x)\,\boldsymbol{e}_x$. Another equally simple example of parallel acoustics is the boundary condition generated by a planar travelling wave of the form $\boldsymbol{v}_1^d = v_{1a}\mathrm{e}^{\mathrm{i}k_0 x}\boldsymbol{e}_x$. Here, only the energy-flux density $\langle \boldsymbol{S}_{\mathrm{ac}\parallel}^d \rangle$ in Eq. (62a) contributes to the streaming velocity which becomes the constant value $\boldsymbol{v}_{2\parallel}^{d0} = (1/4)(v_{1a}^2/c_0)\,\boldsymbol{e}_x$.

The opposite limit is perpendicular acoustics, where the pressure is mainly related to the perpendicular velocity variations $\partial_\zeta v_{1\zeta}^d = \mathrm{i}\omega\kappa_0 p_1$. In this limit, Eq. (61a) is given by a single term

$$\boldsymbol{v}_{2\parallel}^{d0} = -\kappa_0 \langle \boldsymbol{S}_{\mathrm{ac}\parallel}^d \rangle, \quad \text{for perpendicular acoustics, } |\partial_\zeta v_{1\zeta}^d| \gg |\boldsymbol{\nabla}_\parallel \cdot \boldsymbol{v}_{1\parallel}^{d0}|. \tag{62b}$$

We emphasize that in these two limits, the only mechanism that can induce a streaming slip velocity, which rotates parallel to the surface, is the energy-flux density $\langle \boldsymbol{S}_{\mathrm{ac}}^d \rangle$. As seen from Eq. (52b), this mechanism also governs the force density driving streaming in the bulk. In general, $\langle \boldsymbol{S}_{\mathrm{ac}}^d \rangle$ can drive rotating streaming, if it has a nonzero curl. This we compute to lowest order in Γ using Eq. (19b) and $\boldsymbol{\nabla} \times \boldsymbol{v}_1^d = \boldsymbol{0}$, and find it to be proportional to the acoustic angular momentum density,

$$\boldsymbol{\nabla} \times \langle \boldsymbol{S}_{\mathrm{ac}}^d \rangle = \omega^2 \langle \boldsymbol{r}_1^d \times (\rho_0 \boldsymbol{v}_1^d) \rangle, \quad \boldsymbol{r}_1^d = \frac{\mathrm{i}}{\omega} \boldsymbol{v}_1^d. \tag{63}$$

VII. NUMERICAL MODELING IN COMSOL

In the following we implement our extended acoustic pressure theory, Eqs. (20a) and (25) for p_1, and streaming theory, Eqs. (52) and (55) for $\boldsymbol{v}_2^d$ and p_2, in the commercial finite-element-method (FEM) software COMSOL MULTIPHYSICS.[41] We compare these simulations with a full boundary-layer-resolved model for the acoustics, Eqs. (17) and (8a) for $\boldsymbol{v}_1$ and p_1, and for the streaming, Eqs. (34) and (8b) for $\boldsymbol{v}_2$ and p_2. The full model is based on our previous acoustofluidic modeling of fluids-only systems[28,36,42] and solid-fluid systems.[43]

Remarkably, our extended (effective) acoustic pressure model makes it possible to simulate acoustofluidic systems not accessible to the brute-force method of the full model for three reasons: (1) In the full model, the thin boundary layers need to be resolved with a fine FEM mesh. This is not needed in our effective model. (2) For the first-order acoustics, the full model is based on the vector field $\boldsymbol{v}_1$ and the scalar field p_1, whereas our effective model is only based on the scalar field p_1. (3) For the second-order streaming, the full equations (34) contain large canceling terms, which have been removed in the equations (52) used in the effective model. Therefore, also in the bulk, the effective model can be computed on a much coarser FEM mesh than the full model.

In Sec. VIII, we model a fluid domain Ω_{fl} driven by boundary conditions applied directly on $\partial\Omega_{\mathrm{fl}}$, and in Sec. IX, we model a fluid domain Ω_{fl} embedded in an elastic solid domain Ω_{sl} driven by boundary conditions applied on the outer part of the solid boundary $\partial\Omega_{\mathrm{sl}}$.

In COMSOL, we specify user-defined equations and boundary conditions in weak form using the PDE mathematics module, and we express all vector fields in Cartesian coordinates (x, y, z). At the boundary $\partial\Omega_{\mathrm{fl}}$, the local right-handed orthonormal basis $\{\boldsymbol{e}_\xi, \boldsymbol{e}_\eta, \boldsymbol{e}_\zeta\}$ is implemented using the built-in COMSOL tangent vectors `t1` and `t2` as well as the normal vector `n`, all given in Cartesian coordinates. Boundary-layer fields (superscript "0"), such as $\boldsymbol{V}_1^0$, $\boldsymbol{v}_1^{d0}$, and $\boldsymbol{v}_1^{\delta 0}$, are defined on the boundary $\partial\Omega_{\mathrm{fl}}$ only, and their spatial derivatives are computed using the built-in tangent-plane derivative operator `dtang`. For example, in COMSOL we call the Cartesian components of $\boldsymbol{v}_1^{\delta 0}$ for `vdX`, `vdY`, and `vdZ` and compute $\boldsymbol{\nabla} \cdot \boldsymbol{v}_1^{\delta 0}$ as `dtang(vdX,x)+dtang(vdY,y)+dtang(vdZ,z)`. The models are implemented in COMSOL using the following two-step procedure.[36]

Step (1), first-order fields:[42,43] For a given frequency ω, the driving first-order boundary conditions for the system are specified; the wall velocity $\boldsymbol{V}_1^0$ on $\partial\Omega_{\mathrm{fl}}$ for the fluid-only model, and the outer wall displacement $\boldsymbol{u}_1$ on $\partial\Omega_{\mathrm{sl}}$ for the solid-fluid model. Then, the first-order fields are solved; the pressure p_1 in Ω_{fl} using Eqs. (20a) and (25), and, if included in the model, the solid displacement $\boldsymbol{u}_1$ in the solid domain Ω_{sl}.

In particular, in COMSOL we implement $\partial_\zeta^2 p_1 = (\boldsymbol{e}_\zeta \cdot \boldsymbol{\nabla})^2 p_1$ in Eq. (25) as `nx*nx*p1xx + 2*nx*ny*p1xy + ⋯`.

Step (2), second-order fields:[36,42] Time averages $\frac{1}{2}\mathrm{Re}\{f^* g\}$ are implemented using the built-in COMSOL operator `realdot` as `0.5*realdot(f,g)`. Moreover, in the boundary condition (55), the normal derivative of $v_{1\zeta}^d$ in $\boldsymbol{A}$ is rewritten as $\partial_\zeta v_{1\zeta}^d = \boldsymbol{\nabla}\cdot\boldsymbol{v}_1^d - \boldsymbol{\nabla}\cdot\boldsymbol{v}_1^{d0} = \mathrm{i}\kappa_0\omega p_1^0 - \boldsymbol{\nabla}\cdot\boldsymbol{v}_1^{d0}$ for computational ease, and the advective derivatives in $\boldsymbol{A}$ and $\boldsymbol{B}$, such as the term $\mathrm{Re}\{\boldsymbol{v}_1^{\delta 0*}\cdot\boldsymbol{\nabla}\boldsymbol{v}_1^{\delta 0}\}\cdot\boldsymbol{e}_x$ in $\boldsymbol{A}\cdot\boldsymbol{e}_x$, are computed as `realdot(vdX, dtang(vdX,x)) + realdot(vdY,dtang(vdX,y)) + realdot(vdZ,dtang(vdX,z))`.

All numerics were carried out on a workstation, Dell Inc Precision T3610 Intel Xeon CPU E5–1650 v2 at 3.50 GHz with 128 GB RAM and 6 CPU cores.

VIII. EXAMPLE I: A RECTANGULAR CAVITY

We apply our theory to a long, straight channel along the x axis with a rectangular cross section in the vertical y-z plane, a system intensively studied in the literature both theoretically[28,36,42] and experimentally.[25,45–47] We consider the 2D rectangular fluid domain Ω_{fl} with $-\frac{1}{2}W < y < \frac{1}{2}W$ and $-\frac{1}{2}H < z < \frac{1}{2}H$, where the top and bottom walls at $z = \pm\frac{1}{2}H$ are stationary and the vertical side walls at $y = \pm\frac{1}{2}W$ oscillate with a given velocity $V_{1y}^0 w(z)\mathrm{e}^{-\mathrm{i}\omega t}\boldsymbol{e}_y$ and frequency $f = \omega/2\pi$ close to $c_0/2W$, thus exciting a half-wave resonance in the y-direction. In the simulations we choose the wall velocity to be $V_{1y}^0 = d_0\omega$ with a displacement amplitude $d_0 = 0.1$ nm. The material parameters used in the model are shown in Table I.

We compare the results from the effective theory with the full boundary-layer-resolved simulation developed by Muller *et al.*[28] Moreover, we derive analytical expressions for the acoustic fields, using pressure acoustics and our extended boundary condition (25), and for the streaming boundary condition using Eq. (55).

A. First-order pressure

To leading order in ϵ and assuming small variations in z, Eqs. (20a) and (25) in the fluid domain Ω_{fl} become

$$\nabla^2 p_1 + k_0^2 p_1 = 0, \quad \boldsymbol{r}\in\Omega_{\mathrm{fl}}, \tag{64a}$$

TABLE I. Material parameters at 25 °C used in the numerical modeling presented in Secs. VIII and IX.

Water (Ref. 42)			
Mass density	ρ_0	997.05	kg m^{-3}
Compressibility	κ_0	452	TPa^{-1}
Speed of sound	c_0	1496.7	m s^{-1}
Dynamic viscosity	η_0	0.890	mPa s
Bulk viscosity	η_0^{b}	2.485	mPa s
Pyrex glass (Ref. 44)			
Mass density	ρ_{sl}	2230	kg m^{-3}
Speed of sound, longitudinal	c_{lo}	5592	m s^{-1}
Speed of sound, transverse	c_{tr}	3424	m s^{-1}
Solid damping coefficient	Γ_{sl}	0.001	

$$\partial_y p_1 = \mathrm{i}\omega\rho_0 V_{1y}^0 w(z), \quad y = \pm\frac{1}{2}W, \tag{64b}$$

$$\mp\partial_z p_1 = -\frac{\mathrm{i}}{k_{\mathrm{s}}}k_0^2 p_1, \quad z = \pm\frac{1}{2}H. \tag{64c}$$

This problem is solved analytically by separation of variables, introducing k_y and k_z with $k_y^2 + k_z^2 = k_0^2$ and choosing a symmetric velocity envelope function $w(z) = \cos(k_z z)$. The solution is the pressure $p_1 = A\sin(k_y y)\cos(k_z z)$, where A is found from Eq. (64b),

$$p_1(y,z) = \frac{\mathrm{i}\omega\rho_0 V_{1y}^0}{k_y\cos\left(k_y\frac{W}{2}\right)}\sin(k_y y)\cos(k_z z). \tag{65}$$

According to Eq. (64c), k_z must satisfy

$$k_0^2 = \mathrm{i}k_{\mathrm{s}}k_z\tan\left(k_z\frac{H}{2}\right), \tag{66}$$

and using $\tan(k_z H/2)\approx k_z H/2$ for $k_z H \ll 1$, we obtain

$$k_z^2 = -(1+\mathrm{i})\frac{\delta}{H}k_0^2, \quad k_y^2 = \left[1+(1+\mathrm{i})\frac{\delta}{H}\right]k_0^2. \tag{67}$$

Note that the real part of k_y becomes slightly larger than k_0 since the presence of the boundary layers introduces a small variation in the z direction. The half-wave resonance that maximizes the amplitude of p_1 in Eq. (65) is therefore found at a frequency f_{res} slightly lower than $f_{\mathrm{res}}^0 = c_0/2W$,

$$f_{\mathrm{res}} = \left(1-\frac{1}{2}\Gamma_{\mathrm{bl}}\right)f_{\mathrm{res}}^0, \quad \text{with } \Gamma_{\mathrm{bl}} = \frac{\delta}{H}. \tag{68}$$

Here, we introduced the boundary-layer damping coefficient Γ_{bl} that shifts f_{res} away from f_{res}^0. This resonance shift arises from the extended boundary condition (25) and is thus beyond classical pressure acoustics.

Using $f = f_{\mathrm{res}}$ in Eq. (65) and expanding to leading order in Γ_{bl}, gives the resonance pressure and velocity,

$$\frac{p_1^{\mathrm{res}}}{\rho_0 c_0} = -\frac{4V_{1y}^0}{\pi\Gamma_{\mathrm{bl}}}\left\{\sin(\tilde{y}) + \frac{\Gamma_{\mathrm{bl}}}{2}[\mathrm{i}\tilde{y}\cos(\tilde{y}) - (1+\mathrm{i})\sin(\tilde{y})]\right\}Z^{\mathrm{res}}(\tilde{z}), \tag{69a}$$

$$v_{1y}^{d,\mathrm{res}} = \frac{4\mathrm{i}V_{1y}^0}{\pi\Gamma_{\mathrm{bl}}}\left\{\cos(\tilde{y}) - \frac{\Gamma_{\mathrm{bl}}}{2}\mathrm{i}\tilde{y}\sin(\tilde{y})\right\}Z^{\mathrm{res}}(\tilde{z}), \tag{69b}$$

$$v_{1z}^{d,\mathrm{res}} = \frac{4\mathrm{i}V_{1y}^0}{\pi}(1+\mathrm{i})\sin(\tilde{y})\,\tilde{z}, \tag{69c}$$

where $\tilde{y} = \pi(y/W)$, $\tilde{z} = \pi(z/W)$, and $Z_{\mathrm{res}}(\tilde{z}) = 1 + \frac{1}{2}\Gamma_{\mathrm{bl}}(1+\mathrm{i})\tilde{z}^2$. Note that at resonance, the horizontal velocity component is amplified by a factor $\Gamma_{\mathrm{bl}}^{-1}$ relative to the

wall velocity, $v_{1y}^{d,\mathrm{res}} \sim \Gamma_{\mathrm{bl}}^{-1} v_{1z}^{d,\mathrm{res}} \sim \Gamma_{\mathrm{bl}}^{-1} V_{1y}^{0}$, while the horizontal component is not.

In Fig. 2, we compare an effective ("Eff") pressure-acoustics simulation of p_1 solving Eqs. (20a) and (25), with a full pressure-velocity simulation of p_1 and $\boldsymbol{v}_1$ from Eq. (17) as in Muller and Bruus.[28] The analytical results ("Ana") for p_1^{res}, $v_{1y}^{d,\mathrm{res}}$, and $v_{1z}^{d,\mathrm{res}}$ in Eq. (69) are also plotted along the line $y = \frac{1}{4}W$ in Figs. 2(a2), 2(b2), and 2(c2), respectively. The relative deviation between the full and effective fields outside the boundary layer are less than 0.1% even though the latter was obtained using only 5000 degrees of freedom (DoF) on the coarse mesh compared to the 600 000 DoF on the fine mesh for the former. The effective model $\boldsymbol{v}_{1,\mathrm{Eff}}^{d}$ gives the boundary-layer velocity $\boldsymbol{v}_1^{\delta}$ by Eq. (22), and thus by Eq. (18) the complete velocity $\boldsymbol{v}_1 = \boldsymbol{v}_{1,\mathrm{Eff}}^{d} + \boldsymbol{v}_1^{\delta}$ (blue dots in Fig. 2).

To study the resonance behaviour of the acoustic resonator further, we compute the space- and time-averaged energy density $\langle \bar{E}_{\mathrm{ac}}^{d} \rangle$ stored in the acoustic field for frequencies f close to the resonance frequency f_{res}. Inserting $k_y = (\pi/W)(1 + (\mathrm{i}/2)\Gamma_{\mathrm{bl}}) + (2\pi/c_0)(f - f_{\mathrm{res}})$ into Eq. (65), results in the Lorentzian line-shape for $\langle \bar{E}_{\mathrm{ac}}^{d} \rangle$,

$$\begin{aligned}\left\langle \bar{E}_{\mathrm{ac}}^{d} \right\rangle &= \left\langle \bar{E}_{\mathrm{ac}}^{d,\mathrm{kin}} \right\rangle + \left\langle \bar{E}_{\mathrm{ac}}^{d,\mathrm{pot}} \right\rangle = 2\left\langle \bar{E}_{\mathrm{ac}}^{d,\mathrm{pot}} \right\rangle \\ &= \frac{2}{HW} \int\int_{\Omega_{\mathrm{fl}}} \frac{1}{2} \kappa_0 \langle p_1 p_1 \rangle \, \mathrm{d}y\mathrm{d}z \end{aligned} \tag{70a}$$

$$\approx \frac{\frac{1}{\pi^2}\rho_0 \left(V_{1y}^{0}\right)^2}{\left(\frac{f}{f_{\mathrm{res}}} - 1\right)^2 + \left(\frac{1}{2}\Gamma_{\mathrm{bl}}\right)^2}, \quad \text{for } f \approx f_{\mathrm{res}}. \tag{70b}$$

As shown in the graph of $\langle \bar{E}_{\mathrm{ac}}^{d} \rangle$ in Fig. 3, there is full agreement between the effective pressure-acoustics model, the full pressure-velocity model, and the analytical model. In this figure we also show the result obtained using classical pressure acoustics (CPA, gray curves) with $\partial_\zeta p_1 = \mathrm{i}\omega\rho_0 V_{1\zeta}^{0}$ where we see that the boundary layer introduces both damping and shift of the resonance frequency. From the resonance curve follows the maximum energy density at resonance, $\langle \bar{E}_{\mathrm{ac}}^{d,\mathrm{res}} \rangle = \langle \bar{E}_{\mathrm{ac}}^{d}(f_{\mathrm{res}}) \rangle$, and the quality factor Q,

$$\langle \bar{E}_{\mathrm{ac}}^{d,\mathrm{res}} \rangle = \frac{1}{4}\rho_0 \left(\frac{4V_{1y}^{0}}{\pi\Gamma_{\mathrm{bl}}}\right)^2, \quad Q = \frac{1}{\Gamma_{\mathrm{bl}}} = \frac{H}{\delta}. \tag{71}$$

This is also in agreement with the Q-factor in Eq. (33),

$$Q = \frac{2\int\int_{\Omega_{\mathrm{fl}}} \frac{1}{4}\rho_0 |v_{1y}^{\mathrm{res}}|^2 \, \mathrm{d}y\mathrm{d}z}{2\int_{-W/2}^{+W/2} \frac{1}{4}\delta\rho_0 |v_{1y}^{\mathrm{res}}|^2 \, \mathrm{d}y} = \frac{H}{\delta}, \tag{72}$$

which was previously derived by Muller and Bruus[36] and by Hahn *et al.*[38] using the approximation $P_{\mathrm{loss}} \approx P_{\mathrm{visc}}^{\mathrm{diss}}$ in Eq. (33).

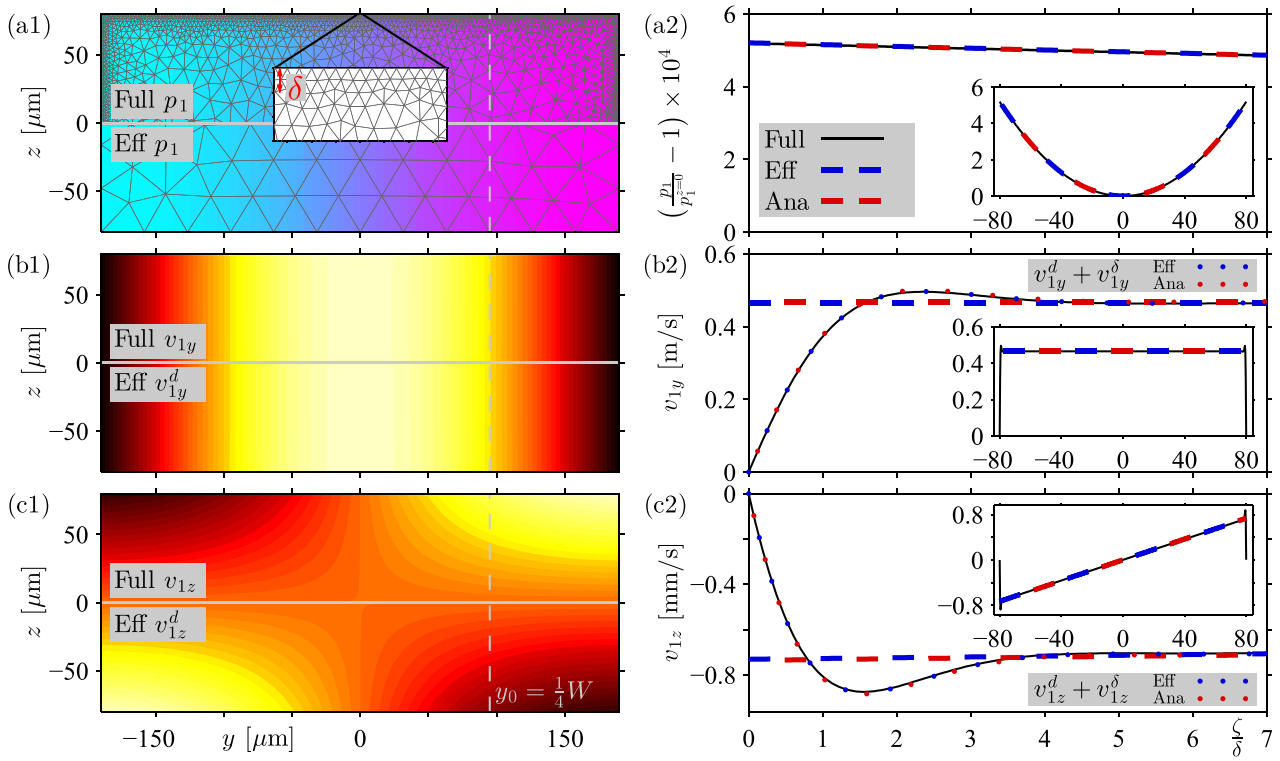

FIG. 2. (Color online) First-order pressure and velocity fields in the vertical rectangular cross section of a long, straight channel of width $W = 380\,\mu$m and height $H = 160\,\mu$m at resonance $f_{\mathrm{res}} = 1.967$ MHz and actuation velocity $V_{1y}^{0} = 2\pi f_{\mathrm{res}} \times 0.1$ nm. Color plots of the full (upper half) and effective (lower half) model fields: (a1) the pressure p_1 from -1 MPa (dark purple) to 1 MPa (light cyan) and the finite element mesh (gray), (b1) the horizontal velocity v_{1y} from 0 m/s (black) to 0.7 m/s (white), and (c1) the vertical velocity v_{1z} from -1 mm/s (black) to 1 mm/s (white). Line plots [Full, Eff, and Ana = analytics from Eq. (69)] at $y_0 = \frac{1}{4}W$ for $-\frac{1}{2}H < z < -\frac{1}{2}H + 7\delta$ (light gray dashed lines) of (a2) the relative pressure deviation $p_1(y_0, z)/p_1(y_0, 0) - 1$, (b2) the horizontal velocity v_{1y}, and (c2) the vertical velocity v_{1z}. Dots are the full velocity (18) $\boldsymbol{v}_1 = \boldsymbol{v}_1^d + \boldsymbol{v}_1^\delta$ with $\boldsymbol{v}_1^\delta$ from Eq. (22) and $\boldsymbol{v}_1^d$ from either "Eff" (dark blue dots) or "Ana" (light red dots). The insets are the corresponding plots along the entire line $-\frac{1}{2}H < z < \frac{1}{2}H$.

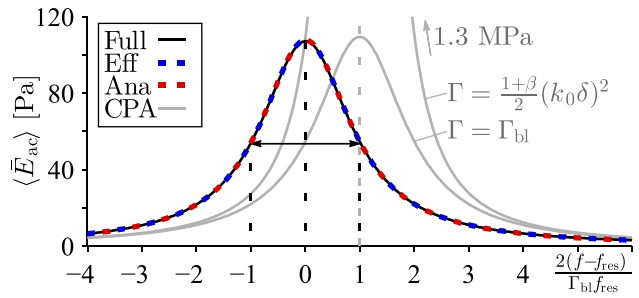

FIG. 3. (Color online) Resonance curves for the rectangular channel. "Ana" refers to the analytical result from Eq. (70b) and "CPA" refers to simulations using classical pressure acoustics with the boundary condition $\partial_\zeta p_1 = i\omega V^0_{1\zeta}$ at $\boldsymbol{r} \in \partial\Omega$ with different choices of bulk damping coefficient Γ.

B. Second-order streaming solution

For the full model at resonance $f_{\rm res}$, we solve Eq. (34), while for the effective model we solve Eq. (52) with the boundary condition on $\boldsymbol{v}_2^d$ obtained by inserting the velocity fields from Eq. (69) into Eq. (54). At the surfaces $z = \pm\frac{1}{2}H$, we find to lowest order in ϵ,

$$v_{2y}^{d0} = \frac{3}{8c_0}\left(\frac{4V_{1y}^0}{\pi\Gamma_{\rm bl}}\right)^2 \sin(2\tilde{y}), \tag{73a}$$

$$v_{2z}^{d0} = \mp(k_0\delta)\frac{1}{8c_0}\left(\frac{4V_{1y}^0}{\pi\Gamma_{\rm bl}}\right)^2 [1 + 10\cos(2\tilde{y})]. \tag{73b}$$

The resulting fields of the two models are shown in Fig. 4. Again, we have good quantitative agreement between the two numerical models, now better than 1% or $3k_0\delta$, for 9000 DoF and 600 000 DoF, respectively.

Analytically, Eq. (73a) is the usual parallel-direction boundary condition for the classical Rayleigh streaming,[22] while Eq. (73b) is beyond that, being the perpendicular-direction boundary condition on the streaming, which is a factor $k_0\delta \approx 3\times10^{-3}$ smaller than the parallel one. This is confirmed in Fig. 4(b) showing the streaming velocity close to $z = -\frac{1}{2}H$ at $y = \frac{1}{4}W$.

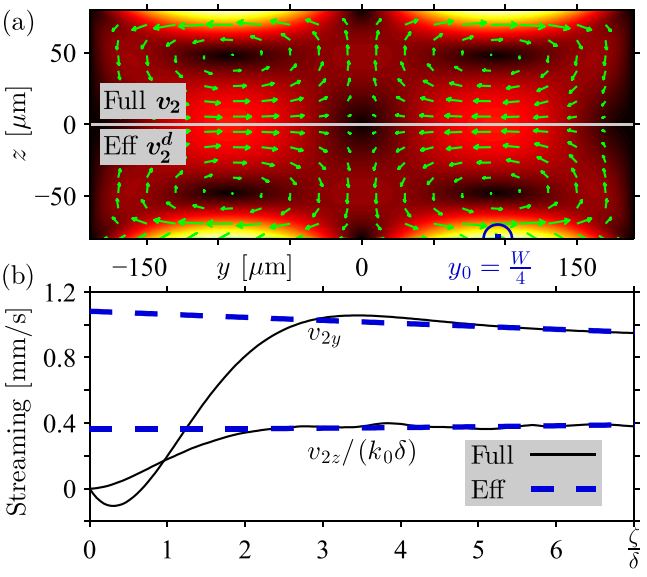

FIG. 4. (Color online) Simulated second-order velocity for the rectangular channel. (a) The full-model $\boldsymbol{v}_2$ (above) and the effective-model $\boldsymbol{v}_2^d$ (below). (b) Line plots near the center of the dark blue half circle in (a) at $y_0 = \frac{1}{4}W$ for $-\frac{1}{2}H < z < -\frac{1}{2}H + 7\delta$.

IX. EXAMPLE II: A CURVED OSCILLATING CAVITY

Next, we implement in COMSOL our boundary conditions (25) and (55) in a system with a curved solid-fluid interface that oscillates in any direction, as described in Sec. VII. We consider an ellipsoidal fluid domain (water) of horizontal major axis $W = 380\,\mu$m and vertical minor axis $H = 160\,\mu$m surrounded by a rectangular solid domain (Pyrex) of width $W_{\rm sl} = 680\,\mu$m and height $H_{\rm sl} = 460\,\mu$m, see Fig. 5. We actuate the solid at its bottom surface using a vertical velocity amplitude $V_z^{\rm act} = d_0\omega\sin(\pi y/W_{\rm sl})$ with $d_0 = 0.1$ nm and at the resonance frequency $f_{\rm res} = 2.222$ MHz, which has

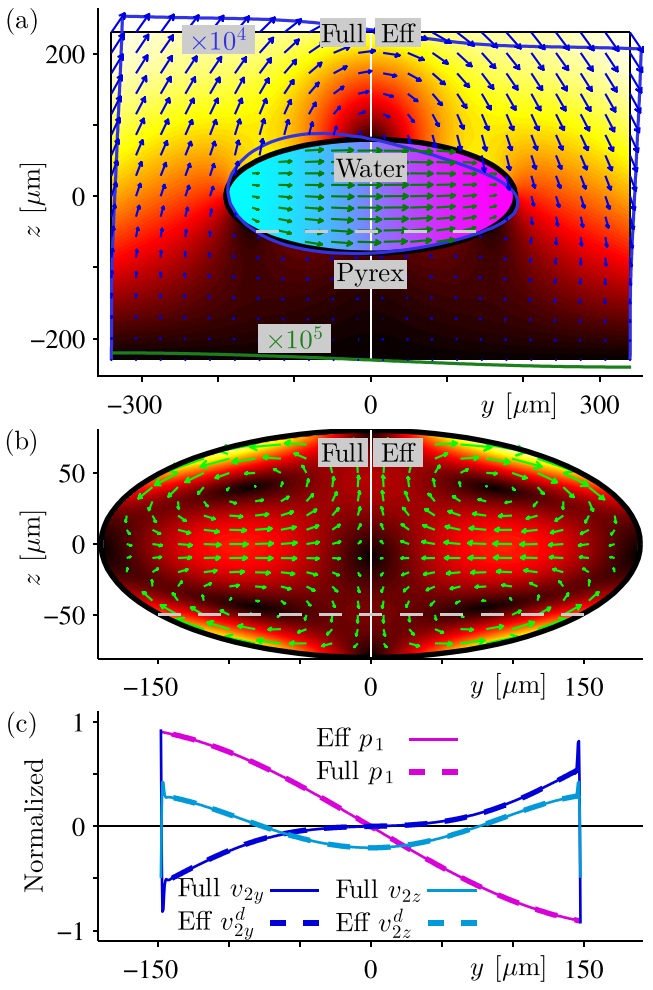

FIG. 5. (Color online) Full (left) and effective (right) simulations for a curved channel with fluid-solid coupling. (a) An elliptic fluid domain with the acoustic pressure p_1 from −0.35 MPa (dark purple) to +0.35 MPa (light cyan) and fluid velocity (green arrows, max 0.2 m/s) surrounded by solid Pyrex with a displacement field $\boldsymbol{u}_{\rm sl}$ (dark blue arrows) and displacement magnitude $|\boldsymbol{u}_{\rm sl}|$ from 0 nm (black) to 2.7 nm (yellow). To be visible, the displacement (dark blue line and dark blue arrows, max 2.7 nm) is enhanced 10^4 times, except at the bottom (green line, max 0.1 nm) where it is enhanced 10^5 times. (b) Streaming velocity $\boldsymbol{v}_2$ (light green arrows) and magnitude from 0 μm/s (black) to 7.8 μm/s (light yellow). (c) Line plots along the light ray dashed line in (a) and (b) of p_1 normalized by 0.35 MPa and $\boldsymbol{v}_2$ by 7.8 μm/s.

been determined numerically as in Fig. 3. The linear governing equations for the displacement field $\boldsymbol{u}_{\mathrm{sl}}$ of the solid are those used by Ley and Bruus,[48]

$$\boldsymbol{\nabla}\cdot\boldsymbol{\sigma}_{\mathrm{sl}} = -\rho_{\mathrm{sl}}\omega^2(1+\mathrm{i}\Gamma_{\mathrm{sl}})\boldsymbol{u}, \quad \text{solid domain}, \tag{74a}$$

$$-\mathrm{i}\omega\boldsymbol{u}_{\mathrm{sl}} = V_z^{\mathrm{act}}(y)\,\boldsymbol{e}_z, \quad \text{actuation at } z=-\frac{1}{2}H_{\mathrm{sl}}, \tag{74b}$$

$$\boldsymbol{n}_{\mathrm{sl}}\cdot\boldsymbol{\sigma}_{\mathrm{sl}} = \boldsymbol{0}, \quad \text{at solid–air interfaces}, \tag{74c}$$

$$\boldsymbol{n}_{\mathrm{sl}}\cdot\boldsymbol{\sigma}_{\mathrm{sl}} = \boldsymbol{n}_{\mathrm{sl}}\cdot\boldsymbol{\sigma}_1, \quad \text{at solid–fluid interfaces}, \tag{74d}$$

where $\boldsymbol{\sigma}_{\mathrm{sl}} = \rho_{\mathrm{sl}}c_{\mathrm{tr}}^2[\boldsymbol{\nabla}\boldsymbol{u}_{\mathrm{sl}} + (\boldsymbol{\nabla}\boldsymbol{u}_{\mathrm{sl}})^T] + \rho_{\mathrm{sl}}(c_{\mathrm{lo}}^2 - 2c_{\mathrm{tr}}^2)(\boldsymbol{\nabla}\cdot\boldsymbol{u}_{\mathrm{sl}})\mathbf{I}$ is the stress tensor of the solid with mass density ρ_{sl}, transverse velocity c_{tr}, longitudinal velocity c_{lo}, and damping coefficient Γ_{sl}, while $\boldsymbol{n}_{\mathrm{sl}}$ is the solid surface normal, and $\boldsymbol{n}_{\mathrm{sl}}\cdot\boldsymbol{\sigma}_1 = \boldsymbol{e}_\zeta\cdot\boldsymbol{\sigma}_1$ is the fluid stress on the solid, Eq. (26). The material parameter values are listed in Table I.

We solve numerically Eqs. (20a) and (25) in first order and Eqs. (52) and (55) in second order. The results are shown in Fig. 5, where we compare the simulation results from the full boundary-layer resolved simulation of Eq. (34) with the effective model. Even for this more complex and realistic system consisting of an elastic solid with a curved oscillating interface coupled to a viscous fluid, we obtain good quantitative agreement between the two numerical models, better than 1% for 600 000 DoF and 9000 DoF, respectively.

X. CONCLUSION

We have studied acoustic pressure and streaming in curved elastic cavities having time-harmonic wall oscillations in any direction. Our analysis relies on the condition that both the surface curvature and wall displacement are sufficiently small as quantified in Eq. (16).

We have developed an extension of the conventional theory of first-order pressure acoustics by including the viscous effects of the thin viscous boundary layer. Based on this theory, we have also derived a slip-velocity boundary condition for the steady second-order acoustic streaming, which allows for efficient computations of the resulting incompressible Stokes flow.

The core of our theory is the decomposition of the first- and second-order fields into long- and short-range fields varying on the large bulk length scale d and the small boundary-layer length scale δ, respectively, see Eqs. (19) and (35). In the physically relevant limits, this velocity decomposition allows for analytical solutions of the boundary-layer fields. We emphasize that in contrast to the conventional second-order matching theory of inner solutions in the boundary layer and outer solutions in the bulk, our long- and short-range, second-order, time-averaged fields co-exist in the boundary layer, but the latter die out exponentially beyond the boundary layer leaving only the former in the bulk.

The main theoretical results of the extended pressure acoustics in Sec. III are the boundary conditions (25) and (26) for the pressure p_1 and the stress $\boldsymbol{\sigma}_1\cdot\boldsymbol{e}_\zeta$ expressed in terms of the pressure p_1 and the velocity $\boldsymbol{V}_1^0$ of the wall. These boundary conditions are to be applied to the governing Helmholtz equation (20a) for p_1, and the gradient form (19b) of the compressional acoustic velocity field $\boldsymbol{v}_1^d$. Furthermore, in Sec. IV, we have used the extended pressure boundary condition to derive an expression for the acoustic power loss P_{loss}, Eq. (32), and the quality factor Q, Eq. (33), for acoustic resonances in terms of boundary-layer and bulk loss mechanisms. The main results of the streaming theory in Sec. V are the governing incompressible Stokes equation (52) for the streaming velocity $\boldsymbol{v}_2^d$ and the corresponding extended boundary condition (55) for the streaming slip velocity $\boldsymbol{v}_2^{d0}$. In this context, we have developed a compact formalism based on the $I_{ab}^{(n)}$-integrals of Eq. (43) to carry out with relative ease the integrations that lead to the analytical expression for $\boldsymbol{v}_2^{d0}$. Last, in Sec. VI, we have applied our extended pressure-acoustics theory to several special cases. We have shown how it leads to predictions that goes beyond previous theoretical results in the literature by Lord Rayleigh,[22] Nyborg,[33] Lee and Wang,[34] and Vanneste and Bühler,[35] while it does agree in the appropriate limits with these results.

The physical interpretation of our extended pressure acoustics theory may be summarized as follows: The fluid velocity $\boldsymbol{v}_1$ is the sum of a compressible velocity $\boldsymbol{v}_1^d$ and an incompressible velocity $\boldsymbol{v}_1^\delta$, where the latter dies out beyond the boundary layer. In general, the tangential component $\boldsymbol{V}_{1\parallel}^0 = \boldsymbol{v}_{1\parallel}^{d0} + \boldsymbol{v}_{1\parallel}^{\delta 0}$ of the no-slip condition at the wall induces a tangential compression of $\boldsymbol{v}_1^\delta$ due to the tangential compression of $\boldsymbol{v}_1^d$ and $\boldsymbol{V}_1^0$. This in turn induces a perpendicular velocity component $v_{1\zeta}^{\delta 0}$ due to the incompressibility of $\boldsymbol{v}_1^\delta$. To fulfil the perpendicular no-slip condition $V_{1\zeta}^0 = v_{1\zeta}^{d0} + v_{1\zeta}^{\delta 0}$, the perpendicular component $v_{1\zeta}^{d0}$ of the acoustic velocity must therefore match not just the wall velocity $V_{1\zeta}^0$, as in classical pressure acoustics, but the velocity difference $V_{1\zeta}^0 - v_{1\zeta}^{\delta 0}$. The inclusion of $v_{1\zeta}^{\delta 0}$ takes into account the power delivered to the acoustic fields by the tangential wall motion, and the power lost from the acoustic fields due to tangential fluid motion. Consequently, by incorporating into the boundary condition an analytical solution of $\boldsymbol{v}_1^\delta$, our theory leads to the correct acoustic fields, resonance frequencies, resonance Q-factors, and acoustic streaming.

In Secs. VII–IX we have demonstrated the implementation of our extended acoustic pressure theory in numerical finite-element COMSOL models, and we have presented the results of two specific models in 2D: a water domain with a rectangular cross section and a given velocity actuation on the domain boundary, and a water domain with an elliptic cross section embedded in a rectangular glass domain that is actuated on the outer boundary. By restricting our examples to 2D, we have been able to perform direct numerical simulations of the full boundary-layer-resolved model, and to use these results for validation of our extended acoustic pressure and streaming theory. Remarkably, we have found that even in 2D, our approach makes it possible to simulate acousto-fluidic systems with a drastic nearly 100-fold reduction in the necessary degrees of freedom, while achieving the same quantitative accuracy, typically of order $k_0\delta$, compared to direct numerical simulations of the full boundary-layer resolved model. We have identified three reasons for this

reduction: (1) Neither our first-order nor our second-order method involve the fine-mesh resolution of the boundary layer. (2) Our first-order equations (20a) and (25) requires only the scalar pressure p_1 as an independent variable, while the vector velocity $\boldsymbol{v}_1$ is subsequently computed from p_1, Eq. (19b). (3) Our second-order equations (52) and (55) avoid the numerically demanding evaluation in the entire fluid domain of large terms that nearly cancel, and therefore our method requires a coarser mesh compared to the full model, also in the bulk.

The results from the numerical examples in Secs. VIII and IX show that the extended pressure acoustics theory has the potential of becoming a versatile and very useful tool in the field of acoustofluidics. For the fluid-only rectangular domain in Sec. VIII, we showed how the theory not only leads to accurate numerical results for the acoustic fields and streaming, but also allows for analytical solutions, which correctly predict crucial details related to viscosity of the first-order acoustic resonance, and which open up for a deeper analysis of the physical mechanisms that lead to acoustic streaming. For the coupled fluid-solid system in 2D of an elliptical water domain embedded in a rectangular glass block, we showed in Sec. IX an important example of a more complete and realistic model of an actuated acoustofluidic system. The extended pressure acoustics theory allowed for calculations of acoustic fields and streaming with a relative accuracy lower than 1%. Based on preliminary work in progress in our group, it appears that the extended pressure acoustic theory makes 3D simulations feasible within reasonable memory consumptions for a wide range of microscale acoustofluidic systems such as fluid-filled cavities and channels driven by attached piezoelectric crystals as well as droplets in two-phase systems and on vibrating substrates.

Currently, we have neglected thermal dissipation. It would of course be an obvious and interesting study, to extend the presented theory to include thermoviscous effects. Previous studies[42,49] on acoustofluidic systems with flat walls oscillating only in the perpendicular direction, have shown that the acoustic streaming is unaffected for channels with a height larger than $250\,\delta \approx 100\,\mu$m. We thus expect the predictions of this work to hold for such "high" channels. However, for more flat channels, a significant reduction of the acoustic streaming is predicted, for example a reduction factor of 2 for a channel of height $25\delta \approx 10\ \mu$m.[42] For such "flat" channels, the thermal boundary-layer must be included in our model to ensure reliable predictions. Such an extension of our model seems feasible, as the thermal boundary-layer width is about 3 times smaller than the viscous boundary-layer width for water at 2 MHz and 25 °C. Thus the basic idea of a weakly curved, thin boundary-layer model can be maintained, but of course at the expense of analytical complications arising from including the heat transport equation together with temperature dependence of the material parameters in the presented first- and second-order perturbation theory.

Although we have developed the extended pressure-acoustics theory and corresponding streaming theory within the narrow scope of microscale acoustofluidics, our theories are of general nature and may likely find a much wider use in other branches of acoustics.

APPENDIX A: DIFFERENTIAL GEOMETRY

In the following we present the basic differential geometry used in this work. Because our analysis is carried out in the limit of weakly curved, thin boundary layers, defined by $\epsilon \ll 1$ of Eq. (10) as discussed in Sec. II D, simplifications arise so that we do not need to unfold the full notation of differential geometry based on co- and contravariant derivatives, the metric tensor, and the full Christoffel symbols.[50,51] Instead, we follow the tradition in the field set by Nyborg[33] and by Lee and Wang,[34] and use the vectorial notation based on the unit tangent vectors $\boldsymbol{e}_i$ and the scale factors h_i at position $\boldsymbol{r}$ in the thin boundary layer,

$$\boldsymbol{e}_i = \frac{1}{h_i}\,\partial_i \boldsymbol{r}, \quad \text{with } h_i = |\partial_i \boldsymbol{r}| \quad \text{for } i = \xi, \eta, \zeta, \tag{A1a}$$

$$\boldsymbol{e}_k \cdot \boldsymbol{e}_i = \delta_{ki}, \quad \text{orthonormality by construction.} \tag{A1b}$$

It is natural to introduce the scaled derivatives $\tilde{\partial}_i$ and the curvilinear quantities T_{kji} and $\mathcal{H}_k$,

$$\tilde{\partial}_i = h_i^{-1}\,\partial_i, \quad \text{so that } \boldsymbol{e}_i = \tilde{\partial}_i \boldsymbol{r}, \tag{A2a}$$

$$T_{kji} = (\tilde{\partial}_k \boldsymbol{e}_j) \cdot \boldsymbol{e}_i, \ \text{for } k, j, i = \xi, \eta, \zeta, \tag{A2b}$$

$$\mathcal{H}_k = T_{iki}, \quad \text{sum over repeated index } i. \tag{A2c}$$

T_{kji} is related to, but not identical with, the celebrated Christoffel symbols of differential geometry. The following relations for T_{kji} are useful in the analysis:

$$T_{kji} = T_{jki}, \quad \text{for } i \neq j, \tag{A3a}$$

$$T_{k\xi\xi} = T_{k\eta\eta} = T_{k\zeta\zeta} = 0, \tag{A3b}$$

$$T_{\zeta ji} = 0. \tag{A3c}$$

Equation (A3a) follows from $T_{kji} = (1/h_k)\partial_k((1/h_j)\partial_j \boldsymbol{r}) \cdot \boldsymbol{e}_i = (\partial_k \partial_j \boldsymbol{r}/h_k h_j) \cdot \boldsymbol{e}_i - (\partial_k h_j / h_k h_j)\boldsymbol{e}_j \cdot \boldsymbol{e}_i$, which is symmetric in k and j as the last term is zero for $j \neq i$, Eq. (A3b) is proven by observing $T_{k\xi\xi} = (\tilde{\partial}_k \boldsymbol{e}_\xi) \cdot \boldsymbol{e}_\xi = \frac{1}{2}\tilde{\partial}_k(\boldsymbol{e}_\xi \cdot \boldsymbol{e}_\xi) = 0$ as $\boldsymbol{e}_\xi \cdot \boldsymbol{e}_\xi = 1$, and Eq. (A3c) arises because ζ is defined as the normal direction, and as a consequence T_{kji} is only nonzero for the tangential derivatives $T_{\xi ji}$ and $T_{\eta ji}$, and $\mathcal{H}_k = T_{\xi k\xi} + T_{\eta k\eta}$. It is in this sense that the surface length scale is set by $R \sim \min\{T_{kji}^{-1}, \mathcal{H}_k^{-1}\}$ as stated in Sec. II E.

From now on, we use the index notation, where, as in Eq. (A2c), a repeated index implies a summation. In curvilinear coordinates, the $\boldsymbol{\nabla}$ operator and vector fields are written as

$$\boldsymbol{\nabla} = \boldsymbol{e}_i \tilde{\partial}_i, \quad \boldsymbol{A} = A_i\,\boldsymbol{e}_i, \tag{A4}$$

and from this all other differential operators are calculated. The first example is the Laplacian of a scalar,

$$\begin{aligned}\nabla^2 g = \boldsymbol{\nabla} \cdot \boldsymbol{\nabla} g &= (\boldsymbol{e}_j \tilde{\partial}_j) \cdot \boldsymbol{e}_i \tilde{\partial}_i g \\ &= \left[\boldsymbol{e}_j \cdot \boldsymbol{e}_i \tilde{\partial}_j + \boldsymbol{e}_j \cdot (\tilde{\partial}_j \boldsymbol{e}_i)\right] \tilde{\partial}_i g \\ &= (\tilde{\partial}_i + T_{jij})\tilde{\partial}_i g = (\tilde{\partial}_i \tilde{\partial}_i + \mathcal{H}_i \tilde{\partial}_i) g.\end{aligned} \tag{A5}$$

The divergence of a vector field $\boldsymbol{A}$ takes the form

$$\begin{aligned}\boldsymbol{\nabla}\cdot\boldsymbol{A} &= \boldsymbol{e}_i\cdot\tilde{\partial}_i(A_k\boldsymbol{e}_k) = \left[(\tilde{\partial}_i A_k)\boldsymbol{e}_k + A_k\tilde{\partial}_i\boldsymbol{e}_k\right]\cdot\boldsymbol{e}_i \\ &= (\tilde{\partial}_i A_k)\delta_{ik} + A_k T_{iki} = (\tilde{\partial}_k + \mathcal{H}_k)A_k, \end{aligned} \tag{A6}$$

while the gradient of a vector field $\boldsymbol{B}$ is

$$\begin{aligned}\boldsymbol{\nabla}\boldsymbol{B} &= \boldsymbol{e}_k\tilde{\partial}_k(B_j\boldsymbol{e}_j) = \boldsymbol{e}_k\left[(\tilde{\partial}_k B_i)\boldsymbol{e}_i + B_j\tilde{\partial}_k\boldsymbol{e}_j\right] \\ &= \boldsymbol{e}_k(\tilde{\partial}_k B_i + T_{kji}B_j)\boldsymbol{e}_i. \end{aligned} \tag{A7}$$

From this follows the advective derivative $(\boldsymbol{A}\cdot\boldsymbol{\nabla})\boldsymbol{B}$ of a vector $\boldsymbol{B}$ with respect to a vector $\boldsymbol{A}$,

$$(\boldsymbol{A}\cdot\boldsymbol{\nabla})\boldsymbol{B} = A_k(\tilde{\partial}_k B_i + T_{kji}B_j)\boldsymbol{e}_i, \tag{A8}$$

and the Laplacian of a vector $\boldsymbol{B}$,

$$\begin{aligned}\nabla^2 B = \boldsymbol{\nabla}\cdot\boldsymbol{\nabla}B &= e_n\tilde{\partial}_n\left[e_k(\tilde{\partial}_k B_i + T_{kji}B_j)e_i\right] \\ &= \mathcal{H}_k(\tilde{\partial}_k B_i + T_{kji}B_j)e_i \\ &\quad + \left[\tilde{\partial}_k\tilde{\partial}_k B_i + B_j\tilde{\partial}_k T_{kji} + T_{kji}\tilde{\partial}_k B_j\right]e_i \\ &\quad + (\tilde{\partial}_k B_i + T_{kji}B_j)T_{kim}e_m. \end{aligned} \tag{A9}$$

In the analysis of fields in the weakly curved, thin boundary layer, it is useful to decompose a given vector $\boldsymbol{A}$ into parallel and perpendicular components,

$$\boldsymbol{A} = \boldsymbol{A}_\parallel + A_\zeta\,\boldsymbol{e}_\zeta, \tag{A10a}$$

$$\boldsymbol{A}_\parallel = A_\xi\,\boldsymbol{e}_\xi + A_\eta\,\boldsymbol{e}_\eta = A_\alpha\,\boldsymbol{e}_\alpha, \tag{A10b}$$

where here and in the following, repeated Greek index α only sums over the tangential indices ξ and η. Likewise, the parallel components of the $\boldsymbol{\nabla}$ operator (A4), the divergence (A6), and the advective derivative (A8) are

$$\boldsymbol{\nabla}_\parallel = \boldsymbol{e}_\alpha\tilde{\partial}_\alpha, \tag{A11a}$$

$$\boldsymbol{\nabla}_\parallel\cdot\boldsymbol{A}_\parallel = (\tilde{\partial}_\alpha + \mathcal{H}_\alpha)A_\alpha, \tag{A11b}$$

$$(\boldsymbol{A}\cdot\boldsymbol{\nabla}_\parallel)\boldsymbol{B} = A_\alpha(\tilde{\partial}_\alpha B_i + T_{\alpha ji}B_j)\boldsymbol{e}_i, \tag{A11c}$$

For the short-ranged boundary-layer vector field $\boldsymbol{A}^\delta = \boldsymbol{A}^{\delta 0}\ (\xi,\eta)\,a^\delta(\zeta)$ introduced in Eq. (14), and the analogous scalar field $g^\delta = g^{\delta 0}(\xi,\eta)\,a^\delta(\zeta)$, the derivative expressions simplifies in the weakly curved thin boundary-layer limit $\epsilon \ll 1$. The reason is that terms containing surface-derivative quantities $\boldsymbol{\nabla}_\parallel$, T_{kji}, and $\mathcal{H}_k$, all of size d^{-1}, are a factor of ϵ smaller than terms with the perpendicular derivative $\tilde{\partial}_\zeta = \partial_\zeta$, which picks up a factor of δ^{-1} due to the factor $a^\delta(\zeta)$ that decays on the length scale δ.

For $\nabla^2 g^\delta$ in Eq. (A5), the first term $\tilde{\partial}_i\tilde{\partial}_i g^\delta = \partial_\zeta^2 g^\delta \sim \delta^{-2}g^\delta$ is ϵ^{-1} larger than the second term $\mathcal{H}_i\tilde{\partial}_i g^\delta \sim R^{-1}\delta^{-1}g^\delta$, so that $\nabla^2 g^\delta \approx \partial_\zeta^2 g^\delta$ as stated in Eq. (15a).

Similarly, for $\nabla^2\boldsymbol{A}^\delta$ in Eq. (A9), the only term that does not contain at least one factor $\mathcal{H}_k$ or T_{kji} is $(\tilde{\partial}_k\tilde{\partial}_k A_i^\delta)\,\boldsymbol{e}_i \approx (\partial_\zeta^2 A_i^\delta)\,\boldsymbol{e}_i = \partial_\zeta^2\boldsymbol{A}^\delta$ as stated in Eq. (15b).

Finally, for Eq. (A6), $\tilde{\boldsymbol{\nabla}}\cdot\boldsymbol{A}^\delta = \boldsymbol{\nabla}_\parallel\cdot\boldsymbol{A}_\parallel^\delta + (\tilde{\partial}_\zeta + \mathcal{H}_\zeta)A_\zeta^\delta \approx \boldsymbol{\nabla}_\parallel\cdot\boldsymbol{A}_\parallel^\delta + \partial_\zeta A_\zeta^\delta$ as stated in Eq. (15c).

APPENDIX B: ACOUSTIC POWER BALANCE

The time averages $\langle E_{\mathrm{ac}}^{\mathrm{kin}}\rangle$, $\langle E_{\mathrm{ac}}^{\mathrm{pot}}\rangle$, and $\langle E_{\mathrm{ac}}\rangle$ of the kinetic, the potential, and the total acoustic energy density, respectively, are given by

$$\langle E_{\mathrm{ac}}^{\mathrm{kin}}\rangle = \frac{1}{2}\rho_0\langle\boldsymbol{v}_1\cdot\boldsymbol{v}_1\rangle, \tag{B1a}$$

$$\langle E_{\mathrm{ac}}^{\mathrm{pot}}\rangle = \frac{1}{2}\kappa_0\langle p_1 p_1\rangle, \tag{B1b}$$

$$\langle E_{\mathrm{ac}}\rangle = \langle E_{\mathrm{ac}}^{\mathrm{kin}}\rangle + \langle E_{\mathrm{ac}}^{\mathrm{pot}}\rangle. \tag{B1c}$$

Using Gauss's theorem and $\rho_0\partial_t\boldsymbol{v}_1 = \boldsymbol{\nabla}\cdot\boldsymbol{\sigma}_1$, the time-averaged total power delivered by the surrounding wall is written as the sum of the time-averaged rate of change of the acoustic energy and total power dissipated into heat,

$$\oint_{\partial\Omega}\langle\boldsymbol{V}_1^0\cdot\boldsymbol{\sigma}_1\rangle\cdot\boldsymbol{n}\,\mathrm{d}A$$

$$= \int_\Omega\boldsymbol{\nabla}\cdot\langle\boldsymbol{v}_1\cdot\boldsymbol{\sigma}_1\rangle\,\mathrm{d}V \tag{B2a}$$

$$= \int_\Omega[\langle\boldsymbol{v}_1\cdot(\boldsymbol{\nabla}\cdot\boldsymbol{\sigma}_1)\rangle + \langle(\boldsymbol{\nabla}\boldsymbol{v}_1)\,:\boldsymbol{\sigma}_1\rangle]\mathrm{d}V \tag{B2b}$$

$$= \int_\Omega[\langle\partial_t E_{\mathrm{ac}}\rangle + \langle(\boldsymbol{\nabla}\boldsymbol{v}_1)\,:\boldsymbol{\tau}_1\rangle]\mathrm{d}V. \tag{B2c}$$

Solving for the time-averaged change in acoustic energy $\int_\Omega\langle\partial_t E_{\mathrm{ac}}\rangle\mathrm{d}V$ in Eq. (B2c) gives

$$\int_\Omega\langle\partial_t E_{\mathrm{ac}}\rangle\,\mathrm{d}V$$

$$= \oint_{\partial\Omega}\langle\boldsymbol{V}_1^0\cdot\boldsymbol{\sigma}_1\rangle\cdot\boldsymbol{n}\,\mathrm{d}A - \int_\Omega\langle(\boldsymbol{\nabla}\boldsymbol{v}_1)\,:\boldsymbol{\tau}_1\rangle\,\mathrm{d}V \tag{B3a}$$

$$= \oint_{\partial\Omega}\langle\boldsymbol{V}_1^0(-p_1)\rangle\cdot\boldsymbol{n}\,\mathrm{d}A + \int_\Omega\langle\boldsymbol{v}_1\cdot(\boldsymbol{\nabla}\cdot\boldsymbol{\tau}_1)\rangle\,\mathrm{d}V, \tag{B3b}$$

where Gauss's theorem transforms $\int_{\partial\Omega}\langle\boldsymbol{V}_1^0\cdot\boldsymbol{\tau}_1\rangle\cdot\boldsymbol{n}\,\mathrm{d}A$ into a volume integral, and $\boldsymbol{n} = -\boldsymbol{e}_\zeta$ is the normal vector of the fluid domain Ω. We may interpret the last term in Eq. (B3b) as the rate of change of stored energy due to the viscosity-induced power $\langle P_{\mathrm{visc}}\rangle$,

$$\langle P_{\mathrm{visc}}\rangle = \langle P_{\mathrm{visc}}^{\mathrm{diss}}\rangle + \langle P_{\mathrm{visc}}^{\mathrm{wall}}\rangle. \tag{B4}$$

Here, $\langle P_{\mathrm{visc}}^{\mathrm{diss}}\rangle$ is the viscous power dissipation into heat and $\langle P_{\mathrm{visc}}^{\mathrm{wall}}\rangle$ is the power from the viscous part of the work performed by the wall on the fluid,

$$\langle P_{\mathrm{visc}}\rangle = \int_\Omega\langle\boldsymbol{v}_1\cdot(\boldsymbol{\nabla}\cdot\boldsymbol{\tau}_1)\rangle\mathrm{d}V, \tag{B5a}$$

$$\langle P_{\rm visc}^{\rm diss}\rangle = -\int_\Omega \langle(\boldsymbol{\nabla}\cdot\boldsymbol{v}_1) : \boldsymbol{\tau}_1\rangle\,\mathrm{d}V, \tag{B5b}$$

$$\langle P_{\rm visc}^{\rm wall}\rangle = \oint_{\partial\Omega} \langle \boldsymbol{v}_1 \cdot \boldsymbol{\tau}_1\rangle \cdot \boldsymbol{n}\,\mathrm{d}A. \tag{B5c}$$

Using Eqs. (18) and (19) we evaluate $\langle P_{\rm visc}\rangle$,

$$\langle P_{\rm visc}\rangle = \int_\Omega \langle \boldsymbol{v}_1 \cdot (\boldsymbol{\nabla}\cdot\boldsymbol{\tau}_1)\rangle\,\mathrm{d}V \tag{B6a}$$

$$= \int_\Omega \langle \boldsymbol{v}_1 \cdot (\mathrm{i}\Gamma\boldsymbol{\nabla}p_1 - \mathrm{i}\omega\rho_0\boldsymbol{v}_1^\delta)\rangle\,\mathrm{d}V \tag{B6b}$$

$$= \int_\Omega \left[-\frac{\Gamma\omega\rho_0}{2}|\boldsymbol{v}_1^d|^2 + \langle \partial_t E_{\rm ac}^{{\rm kin},\delta}\rangle\right]\mathrm{d}V - \oint_{\partial\Omega}\langle p_1\boldsymbol{v}_1^{\delta 0}\rangle \cdot \boldsymbol{n}\,\mathrm{d}A, \tag{B6c}$$

where we used Eq. (19) and Gauss's theorem. Inserting Eq. (B6c) into Eq. (B3b) leads to Eq. (30). Comparing with Eq. (32), we can relate $\langle P_{\rm loss}\rangle = \langle P_{\rm loss}^d\rangle$ and $\langle P_{\rm visc}\rangle$,

$$\langle P_{\rm loss}\rangle = \langle P_{\rm visc}\rangle - \oint_{\partial\Omega}\left\langle p_1\left[\frac{\mathrm{i}}{k_{\rm s}}\boldsymbol{\nabla}_\parallel\cdot\boldsymbol{V}_{1\parallel}^0\right]\right\rangle\cdot\boldsymbol{n}\,\mathrm{d}A \tag{B7a}$$

$$= \langle P_{\rm visc}^{\rm diss}\rangle + \langle P_{\rm visc}^{\rm wall}\rangle - \oint_{\partial\Omega}\left\langle p_1\left[\frac{\mathrm{i}}{k_{\rm s}}\boldsymbol{\nabla}_\parallel\cdot\boldsymbol{V}_{1\parallel}^0\right]\right\rangle\cdot\boldsymbol{n}\,\mathrm{d}A. \tag{B7b}$$

Note that $\langle P_{\rm loss}\rangle$ is not in general the same as the power $\langle P_{\rm visc}^{\rm diss}\rangle$ dissipated into heat. These might, however, be approximately equal if the power

$$\oint_{\partial\Omega} -\langle p_1\boldsymbol{V}_1^0\rangle\cdot\boldsymbol{n}\,\mathrm{d}A$$

delivered by the pressure is approximately balanced by dissipation $\langle P_{\rm visc}^{\rm diss}\rangle$. This happens, if

$$\oint_{\partial\Omega} -\langle p_1\boldsymbol{V}_1^0\rangle\cdot\boldsymbol{n}\,\mathrm{d}A$$

is much larger than $\langle P_{\rm visc}^{\rm wall}\rangle$ and

$$\oint_{\partial\Omega}\left\langle p_1\left[\frac{\mathrm{i}}{k_{\rm s}}\boldsymbol{\nabla}_\parallel\cdot\boldsymbol{V}_{1\parallel}^0\right]\right\rangle\cdot\boldsymbol{n}\,\mathrm{d}A,$$

which is usually satisfied.

APPENDIX C: COMPARISON WITH PREVIOUS RESULTS IN THE LITERATURE

1. Comparison with Lee and Wang (1989)

In the following we rewrite the ξ-component $v_{2\xi}^{d0}$ of the streaming velocity in Eq. (58a) using the notation of Lee and Wang[34] to compare it directly with u_L given in their Eq. $(19)^{\rm LW}$. First, we take the complex conjugate of the argument of the real value, set $\beta=\xi$, and write explicitly the sum over the repeated index $\alpha=\xi,\eta$,

$$\begin{aligned} v_{2\xi}^{d0} = -\frac{1}{4\omega}\mathrm{Re}\Big\{ & v_{1\xi}^{d0}\left(\tilde\partial_\xi v_{1\xi}^{d0*}\right) + v_{1\xi}^{d0}v_{1\eta}^{d0*}T_{\xi\eta\xi} \\ & + v_{1\eta}^{d0}\left(\tilde\partial_\eta v_{1\xi}^{d0*}\right) + v_{1\eta}^{d0}v_{1\eta}^{d0*}T_{\eta\eta\xi} + \big[(2+\mathrm{i})\boldsymbol{\nabla}\cdot\boldsymbol{v}_1^d \\ & - (2+3\mathrm{i})\partial_\zeta v_{1\zeta}^d - (2-\mathrm{i})\mathcal{H}_\zeta V_{1\zeta}^{0*}\big]v_{1\xi}^{d*} \\ & -2\mathrm{i}V_{1\zeta}^{0*}\left(\partial_\zeta v_{1\xi}^d + v_{1\xi}^{d0}T_{\xi\zeta\xi} + v_{1\eta}^{d0}T_{\eta\zeta\xi}\right)\Big\}. \end{aligned} \tag{C1}$$

This expression is rewritten using the notation of Lee and Wang, $\boldsymbol{v}_1^d=\boldsymbol{u}_{a0}$, $(v_{1\xi}^{d0},v_{1\eta}^{d0},v_{1\zeta}^{d0})=(u_{a0},v_{a0},w_{a0})$, $(\xi,\eta,\zeta)=(x,y,z)$, $\mathcal{H}_\zeta=H$, $(\tilde\partial_\xi,\tilde\partial_\eta,\tilde\partial_\zeta)=(\partial_{x_1},\partial_{x_2},\partial_{x_3})$, $T_{kji}=T_{ijk}^{\rm LW}$, and $V_{1\zeta}^0=w_{a0}+\mathcal{O}(\epsilon)$,

$$\begin{aligned} v_{2\xi}^{d0} &= -\frac{1}{4\omega}\mathrm{Re}\big\{u_{a0}\big[\partial_{x_1}u_{a0}^* + v_{a0}^*T_{121}^{\rm LW}\big] \\ &\quad + v_{a0}\big[\partial_{x_2}u_{a0}^* + v_{a0}^*T_{122}^{\rm LW} + u_{a0}^*[(2+\mathrm{i})\boldsymbol{\nabla}\cdot\boldsymbol{u}_{a0} \\ &\quad - (2+3\mathrm{i})\partial_z w_{a0} - (2-\mathrm{i})Hw_{a0}]\big] \\ &\quad - 2\mathrm{i}w_{a0}^*\left(\partial_z u_{a0} + u_{a0}T_{131}^{\rm LW} + v_{a0}T_{132}^{\rm LW}\right)\big\} \\ &= -\frac{1}{4\omega}\mathrm{Re}\big\{q_x + u_{a0}^*[(2+\mathrm{i})\boldsymbol{\nabla}\cdot\boldsymbol{u}_{a0} \\ &\quad - (2+3\mathrm{i})\partial_z w_{a0} - (2-\mathrm{i})Hw_{a0}] \\ &\quad - 2\mathrm{i}w_{a0}^*\left(\partial_z u_{a0} + u_{a0}T_{131}^{\rm LW} + v_{a0}T_{132}^{\rm LW}\right)\big\} \\ &= u_L + \frac{1}{2\omega}\mathrm{Re}\big\{\mathrm{i}w_{a0}^*\left(\partial_z u_{a0} + u_{a0}T_{131}^{\rm LW} + v_{a0}T_{132}^{\rm LW}\right)\big\}. \end{aligned} \tag{C2}$$

Here, we have used the definition of q_x in Eq. $(3)^{\rm LW}$ and the result in Eq. $(19)^{\rm LW}$ for the x-component u_L of the streaming velocity just outside the boundary layer.

Similarly, we obtain for the η-component $v_{2\eta}^{d0}$ in Eq. (58a),

$$v_{2\eta}^{d0} = v_L + \frac{1}{2\omega}\mathrm{Re}\big\{\mathrm{i}w_{a0}^*\left(\partial_z v_{a0} + u_{a0}T_{231}^{\rm LW} + v_{a0}T_{232}^{\rm LW}\right)\big\}, \tag{C3}$$

where we have used the definition in Eq. $(4)^{\rm LW}$ for q_y and the result in Eq. $(20)^{\rm LW}$ for the y-component v_L of the streaming velocity. The comparison obtained in Eqs. (C2) and (C3) is discussed in Sec. VI A.

2. Comparison with Vanneste and Bühler (2011)

In the following we rewrite the ξ-component $v_{2\xi}^{d0}$ of the Eulerian streaming velocity in Eq. (59b) using the notation of Vanneste and Bühler[35] to compare it directly with the Lagrangian streaming velocity $\bar u_{\rm slip}^{\rm L}$ given in their Eq. $(4.10)^{\rm VB}$. First, given the flat wall, $(\xi,\eta,\zeta)=(x,y,z)$ and for all i,j,k we have $h_i=1$, $\mathcal{H}_i=0$, and $T_{ijk}=0$. Then, we identify our first-order velocity fields with theirs: From Eqs. $(2.6)^{\rm VB}$ and $(3.1)^{\rm VB}$ follows $\boldsymbol{v}_1^d=2\boldsymbol{\nabla}\hat\phi$, and from Eqs. $(3.9)^{\rm VB}$ and $(3.10)^{\rm VB}$ we read that $\boldsymbol{v}_{1\parallel}^{\delta 0}=-2\hat U\boldsymbol{e}_x\ -2\hat V\boldsymbol{e}_y$. Next, we relate our steady Eulerian second-order velocity $\boldsymbol{v}_2^d$ with their Lagrangian mean flow $\bar u_{\rm slip}^{\rm L}$ Eq. $(4.10)^{\rm VB}$. Using $\mathrm{Re}Z=\frac{1}{2}Z+\text{c.c.}=\frac{1}{2}Z^*+\text{c.c.}$, we obtain

$$
\begin{aligned}
v_{2\xi}^{d0} &= -\frac{1}{4\omega}\mathrm{Re}\Big\{(1-2\mathrm{i})v_{1\alpha}^{\delta 0*}\partial_\alpha v_{1\xi}^{\delta 0} - 4\mathrm{i}v_{1\alpha}^{\delta 0*}\partial_\alpha v_{1\xi}^{d0} + \Big[(2+\mathrm{i})\partial_\alpha v_{1\alpha}^{\delta 0*} + 2\mathrm{i}\Big(\partial_\alpha v_{1\alpha}^{d0*} - \partial_\zeta v_{1\zeta}^{d*}\Big)\Big]v_{1\xi}^{\delta 0} - 2\mathrm{i}\, v_{1k}^{d*}\partial_k v_{1\xi}^{d}\Big\} \\
&= -\frac{1}{2\omega}\Big\{(1+2\mathrm{i})\hat{U}\partial_x\hat{U}^* + (1+2\mathrm{i})\hat{V}\partial_y\hat{U}^* + 4\mathrm{i}\hat{U}^*\partial_x^2\hat{\phi} + 4\mathrm{i}\hat{V}^*\partial_x\partial_y\hat{\phi} \\
&\quad + \Big[(2+\mathrm{i})\partial_x\hat{U}^* + (2+\mathrm{i})\partial_y\hat{V}^* + 2\mathrm{i}\Big(\partial_x^2\hat{\phi} + \partial_y^2\hat{\phi} - \partial_z^2\hat{\phi}\Big)\Big]\hat{U}^*\Big\} + \mathrm{c.c.} - \frac{1}{\omega}\big\langle \mathrm{i}\boldsymbol{v}_1^{\mathrm{d}}\cdot\boldsymbol{\nabla}\boldsymbol{v}_1^{\mathrm{d}}\big\rangle \\
&= -\frac{1}{2\omega}\Big\{3(1+\mathrm{i})\hat{U}\partial_x\hat{U}^* + (1+2\mathrm{i})\hat{V}\partial_y\hat{U}^* + (2+\mathrm{i})\hat{U}\partial_y\hat{V}^*\Big\} - \frac{\mathrm{i}}{\omega}\Big\{2\partial_x\partial_y\hat{\phi}\hat{V}^* + \Big(\partial_x^2\hat{\phi} + \partial_y^2\hat{\phi} - \partial_z^2\hat{\phi}\Big)\hat{U}^*\Big\} + \mathrm{c.c.} - \hat{\mathrm{u}}^{\mathrm{S}} \\
&= u_{\mathrm{slip}}^{\mathrm{L}} - \hat{u}^{\mathrm{S}} = u_{\mathrm{slip}}^{\mathrm{E}}.
\end{aligned}
\tag{C4}
$$

Here, we have used that the Lagrangian velocity $u_{\mathrm{slip}}^{\mathrm{L}}$, calculated by Vanneste and Bühler in their Eq. $(4.10)^{\mathrm{VB}}$, is related to the Eulerian velocity $u_{\mathrm{slip}}^{\mathrm{E}}$ through the Stokes drift velocity $\hat{u}^{\mathrm{S}} = (1/\omega)\langle \mathrm{i}\boldsymbol{v}_1^d\cdot\boldsymbol{\nabla}\boldsymbol{v}_1^d\rangle$ of Eq. (34c).

Similarly, for the y component $v_{2\eta}^{d0}$ of the streaming,

$$
v_{2\eta}^{d0} = v_{\mathrm{slip}}^{\mathrm{L}} - \hat{v}^{\mathrm{S}} = v_{\mathrm{slip}}^{\mathrm{E}}. \tag{C5}
$$

The comparison obtained in Eqs. (C4) and (C5) is discussed in Sec. VI B.

[1]H. Bruus, J. Dual, J. Hawkes, M. Hill, T. Laurell, J. Nilsson, S. Radel, S. Sadhal, and M. Wiklund, "Forthcoming lab on a chip tutorial series on acoustofluidics: Acoustofluidics-exploiting ultrasonic standing wave forces and acoustic streaming in microfluidic systems for cell and particle manipulation," Lab Chip **11**(21), 3579–3580 (2011).

[2]T. Laurell and A. Lenshof, *Microscale Acoustofluidics* (Royal Society of Chemistry, Cambridge, 2015).

[3]P. Thevoz, J. D. Adams, H. Shea, H. Bruus, and H. T. Soh, "Acoustophoretic synchronization of mammalian cells in microchannels," Anal. Chem. **82**(7), 3094–3098 (2010).

[4]P. Augustsson, C. Magnusson, M. Nordin, H. Lilja, and T. Laurell, "Microfluidic, label-free enrichment of prostate cancer cells in blood based on acoustophoresis," Anal. Chem. **84**(18), 7954–7962 (2012).

[5]P. Augustsson, J. T. Karlsen, H.-W. Su, H. Bruus, and J. Voldman, "Iso-acoustic focusing of cells for size-insensitive acousto-mechanical phenotyping," Nat. Commun. **7**, 11556 (2016).

[6]X. Ding, S.-C. S. Lin, B. Kiraly, H. Yue, S. Li, I.-K. Chiang, J. Shi, S. J. Benkovic, and T. J. Huang, "On-chip manipulation of single microparticles, cells, and organisms using surface acoustic waves," Proc. Natl. Acad. Sci. U.S.A. **109**(28), 11105–11109 (2012).

[7]D. J. Collins, B. Morahan, J. Garcia-Bustos, C. Doerig, M. Plebanski, and A. Neild, "Two-dimensional single-cell patterning with one cell per well driven by surface acoustic waves," Nat. Commun. **6**, 8686 (2015).

[8]B. Hammarström, M. Evander, H. Barbeau, M. Bruzelius, J. Larsson, T. Laurell, and J. Nillsson, "Non-contact acoustic cell trapping in disposable glass capillaries," Lab Chip **10**(17), 2251–2257 (2010).

[9]B. Hammarström, T. Laurell, and J. Nilsson, "Seed particle enabled acoustic trapping of bacteria and nanoparticles in continuous flow systems," Lab Chip **12**, 4296–4304 (2012).

[10]B. Hammarström, M. Evander, J. Wahlström, and J. Nilsson, "Frequency tracking in acoustic trapping for improved performance stability and system surveillance," Lab Chip **14**, 1005–1013 (2014).

[11]B. W. Drinkwater, "Dynamic-field devices for the ultrasonic manipulation of microparticles," Lab Chip **16**, 2360–2375 (2016).

[12]D. J. Collins, C. Devendran, Z. Ma, J. W. Ng, A. Neild, and Y. Ai, "Acoustic tweezers via sub-time-of-flight regime surface acoustic waves," Sci. Adv. **2**(7), e1600089 (2016).

[13]H. G. Lim, Y. Li, M.-Y. Lin, C. Yoon, C. Lee, H. Jung, R. H. Chow, and K. K. Shung, "Calibration of trapping force on cell-size objects from ultrahigh-frequency single-beam acoustic tweezer," IEEE Trans. Ultrason. Ferroelectr. Freq. Control **63**(11), 1988–1995 (2016).

[14]D. Baresch, J.-L. Thomas, and R. Marchiano, "Observation of a single-beam gradient force acoustical trap for elastic particles: Acoustical tweezers," Phys. Rev. Lett. **116**, 024301 (2016).

[15]L. V. King, "On the acoustic radiation pressure on spheres," Proc. R. Soc. London, Ser. A **147**(861), 212–240 (1934).

[16]K. Yosioka and Y. Kawasima, "Acoustic radiation pressure on a compressible sphere," Acustica **5**, 167–173 (1955).

[17]A. A. Doinikov, "Acoustic radiation force on a spherical particle in a viscous heat-conducting fluid. I. General formula," J. Acoust. Soc. Am. **101**(2), 713–721 (1997).

[18]A. A. Doinikov, "Acoustic radiation force on a spherical particle in a viscous heat-conducting fluid. II. Force on a rigid sphere," J. Acoust. Soc. Am. **101**(2), 722–730 (1997).

[19]A. A. Doinikov, "Acoustic radiation force on a spherical particle in a viscous heat-conducting fluid. III. Force on a liquid drop," J. Acoust. Soc. Am. **101**(2), 731–740 (1997).

[20]M. Settnes and H. Bruus, "Forces acting on a small particle in an acoustical field in a viscous fluid," Phys. Rev. E **85**, 016327 (2012).

[21]J. T. Karlsen and H. Bruus, "Forces acting on a small particle in an acoustical field in a thermoviscous fluid," Phys. Rev. E **92**, 043010 (2015).

[22]Lord Rayleigh, "On the circulation of air observed in Kundt's tubes, and on some allied acoustical problems," Philos. Trans. R. Soc. London **175**, 1–21 (1884).

[23]H. Schlichting, "Berechnung ebener periodischer grenzeschichtströmungen," Phys. Z. **33**, 327–335 (1932).

[24]M. Wiklund, R. Green, and M. Ohlin, "Acoustofluidics 14: Applications of acoustic streaming in microfluidic devices," Lab Chip **12**, 2438–2451 (2012).

[25]P. B. Muller, M. Rossi, A. G. Marin, R. Barnkob, P. Augustsson, T. Laurell, C. J. Kähler, and H. Bruus, "Ultrasound-induced acoustophoretic motion of microparticles in three dimensions," Phys. Rev. E **88**(2), 023006 (2013).

[26]J. Lei, P. Glynne-Jones, and M. Hill, "Modal Rayleigh-like streaming in layered acoustofluidic devices," Phys. Fluids **28**, 012004 (2016).

[27]A. Riaud, M. Baudoin, O. Bou Matar, L. Becerra, and J.-L. Thomas, "Selective manipulation of microscopic particles with precursor swirling Rayleigh waves," Phys. Rev. Appl. **7**, 024007 (2017).

[28]P. B. Muller, R. Barnkob, M. J. H. Jensen, and H. Bruus, "A numerical study of microparticle acoustophoresis driven by acoustic radiation forces and streaming-induced drag forces," Lab Chip **12**, 4617–4627 (2012).

[29]R. Barnkob, P. Augustsson, T. Laurell, and H. Bruus, "Acoustic radiation- and streaming-induced microparticle velocities determined by microparticle image velocimetry in an ultrasound symmetry plane," Phys. Rev. E **86**, 056307 (2012).

[30]M. Antfolk, P. B. Muller, P. Augustsson, H. Bruus, and T. Laurell, "Focusing of sub-micrometer particles and bacteria enabled by two-dimensional acoustophoresis," Lab Chip **14**, 2791–2799 (2014).

[31]Z. Mao, P. Li, M. Wu, H. Bachman, N. Mesyngier, X. Guo, S. Liu, F. Costanzo, and T. J. Huang, "Enriching nanoparticles via acoustofluidics," ACS Nano **11**(1), 603–612 (2017).

[32]M. Wu, Z. Mao, K. Chen, H. Bachman, Y. Chen, J. Rufo, L. Ren, P. Li, L. Wang, and T. J. Huang, "Acoustic separation of nanoparticles in continuous flow," Adv. Funct. Mater. **27**(14), 1606039 (2017).

[33]W. L. Nyborg, "Acoustic streaming near a boundary," J. Acoust. Soc. Am. **30**(4), 329–339 (1958).

[34]C. Lee and T. Wang, "Near-boundary streaming around a small sphere due to 2 orthogonal standing waves," J. Acoust. Soc. Am. **85**(3), 1081–1088 (1989).

[35]J. Vanneste and O. Bühler, "Streaming by leaky surface acoustic waves," Proc. R. Soc. London, Ser. A **467**(2130), 1779–1800 (2011).

[36]P. B. Muller and H. Bruus, "Theoretical study of time-dependent, ultrasound-induced acoustic streaming in microchannels," Phys. Rev. E **92**, 063018 (2015).
[37]C. E. Bradley, "Acoustic streaming field structure: The influence of the radiator," J. Acoust. Soc. Am. **100**(3), 1399–1408 (1996).
[38]P. Hahn and J. Dual, "A numerically efficient damping model for acoustic resonances in microfluidic cavities," Phys. Fluids **27**, 062005 (2015).
[39]A. Riaud, M. Baudoin, O. Bou Matar, J.-L. Thomas, and P. Brunet, "On the influence of viscosity and caustics on acoustic streaming in sessile droplets: An experimental and a numerical study with a cost-effective method," J. Fluid Mech. **821**, 384–420 (2017).
[40]C. Eckart, "Vortices and streams caused by sound waves," Phys. Rev. **73**, 68–76 (1948).
[41]COMSOL Multiphysics 5.3a (2017), www.comsol.com (Last viewed 3 August 2018).
[42]P. B. Muller and H. Bruus, "Numerical study of thermoviscous effects in ultrasound-induced acoustic streaming in microchannels," Phys. Rev. E **90**(4), 043016 (2014).
[43]M. W. H. Ley and H. Bruus, "Continuum modeling of hydrodynamic particle-particle interactions in microfluidic high-concentration suspensions," Lab Chip **16**(7), 1178–1188 (2016).
[44]CORNING, Houghton Park C-8, Corning, NY 14831, USA, *Glass Silicon Constraint Substrates*, http://www.valleydesign.com/Datasheets/Corning%20Pyrex%207740.pdf (Last viewed April 18, 2018).
[45]R. Barnkob, P. Augustsson, T. Laurell, and H. Bruus, "Measuring the local pressure amplitude in microchannel acoustophoresis," Lab Chip **10**(5), 563–570 (2010).
[46]P. Augustsson, R. Barnkob, S. T. Wereley, H. Bruus, and T. Laurell, "Automated and temperature-controlled micro-PIV measurements enabling long-term-stable microchannel acoustophoresis characterization," Lab Chip **11**(24), 4152–4164 (2011).
[47]R. Barnkob, I. Iranmanesh, M. Wiklund, and H. Bruus, "Measuring acoustic energy density in microchannel acoustophoresis using a simple and rapid light-intensity method," Lab Chip **12**, 2337–2344 (2012).
[48]M. W. H. Ley and H. Bruus, "Three-dimensional numerical modeling of acoustic trapping in glass capillaries," Phys. Rev. Appl. **8**, 024020 (2017).
[49]A. Y. Rednikov and S. S. Sadhal, "Acoustic/steady streaming from a motionless boundary and related phenomena: Generalized treatment of the inner streaming and examples," J. Fluid. Mech. **667**, 426–462 (2011).
[50]E. Kreyszig, *Differential Geometry* (Dover Publications, New York, 1991).
[51]L. D. Landau and E. M. Lifshitz, *The Classical Theory of Fields*, 4th ed. (Butterworth-Heinemann, Oxford, 1980), Vol. 4.